SPECTROSCOPIC INVESTIGATIONS OF ELECTRON TRANSFER PROCESSES AT
DYE-SENSITIZED PHOTOELECTRODES

Yejee Han

A dissertation submitted to the faculty of the University of North Carolina at Chapel Hill in partial fulfillment of the requirements for the degree of Master of Arts in the Department of Chemistry.

Chapel Hill
2017

Approved by:

Gerald Meyer

Jillian Dempsey

Cynthia Schauer

ABSTRACT

Yejee Han: Spectroscopic Investigations of Electron Transfer Processes at Dye-sensitized
Photoelectrodes
(Under the direction of Jillian L. Dempsey)

Over the last century, energy demands have grown quickly due to an increasing global
population. To limit our dependence on fossil fuels, it is desirable to seek environmentally
clean, alternative energy resources. Solar energy is expected to be a good, renewable
energy candidate because of environmental protection. Crystalline silicon-based
photovoltaic devices used most frequently, with solar to electricity conversion efficiencies
of approximately 25%. However, high cost and complicated fabrication processes excluded
conventional silicon-based solar cells from domestic and other commercial applications.
Dye sensitized solar cells (DSSCs) provide a promising low-cost technology for capturing
solar energy. Until recently, researchers have been focused on n-type DSSCs that use a
wide-band-gap n-type semiconductor oxide such as TiO_2 or ZnO. Even though comparably
fewer studies have examined p-type semiconductors, scientific interest has quickly grown
to understand the factors that control the rate of hole photoinjection and to design more
efficient systems.

Core-shell nanoporous electrode has been used in dye-sensitized solar cells (DSSCs) and
dye-sensitized photoelectrosynthesis cells (DSPECs) as one of the most effective strategies
providing energy barrier of recombination process. We have used a core/shell consisting of
an inner core of a SnO_2 and a thin outer shell of TiO_2 prepared by use of atomic layer
deposition (ALD), where the band potential of the shell is more negative than that of the

core. Transient absorption spectroscopy was used to investigate the interfacial charge recombination dynamics to elucidate the dominated mechanism between tunneling and shell-localized BET in different shell thickness architecture. This study will enable us to use as a quantitative guide for ideal core/shell electrodes in optimizing the most efficient solar cells.

TABLE OF CONTENTS

LIST OF TABLES

LIST OF FIGURES

LIST OF SCHEMES

LIST OF ABBREVIATIONS AND SYMBOLS

E_{00} 0-0 energy gap

bpy   2,2$'$ -bipyridine

Abs   Absorbance

Å   Angstrom

ALD   Atomic layer deposition

BET   Back electron transfer

cm   Centimeter

δ   Chemical shift

CB   Conduction band

ECB   Conduction band energy

CV   Cyclic voltammogram

DOS   Density of states

DCM Dichloromethane

-ΔG° Diving force

DSPEC   Dye-sensitized photoelectrosynthesis cell

DSSC   Dye-sensitized solar cell

e$^-$ Electron

k_{ET} Electron transfer rate contant

eVElectron volts

eq Equivalent

λex   Excitation wavelength

Fc Ferrocene

FTO   Fluorine-doped tin oxide

$E°$ Formal potential

FWHM Full-width at half max

ΔG Gibbs free energy

g   Gram

$E_{1/2}$ Half wave potential

HzHertz

ITO   Indium-doped tin oxide

$h\nu$ Irradiation

K Kelvin

kV   kilovolt

τ Lifetime

λ_{max} Maximum absorbance wavelength

MHz Megahertz

MLCT   Metal-to-ligand charge transfer

µm   Micrometer

µM   Micromolar

µs Microsecond

mJMillijoules

mg   Milligram

mL   Milliliter

mm   Millimeter

mM   Millimolar

mmol Millimole

mOD Millioptical density

mV   Millivolts

M Molar

nm   Nanometer

ns Nanosecond

Nd:YAG   Neodymium doped yttrium aluminum garnet

NiO   Nickel oxide

NHE Normal hydrogen electrode

NMR Nuclear magnetic resonance

λ_{obs} Observation wavelength

Ω Ohm

OCP Open circuit potential

OD   Optical density

OPO Optical parametric oscillator

ppm   Parts per million

PL Photoluminescence

PMT Photomulitplier tube

PS Photosensitizer

PV   Photovoltaic

H^+ Proton

λ Reorganization energy

RuCH$_2$P [Ru(bpy)$_2$(4,4'-(CH$_2$PO$_3$H$_2$)2bpy)]$^{2+}$

s   Second

Γ   Surface coverage

TCO Transparent conductive oxide

T   Temperature

TW   Terawatt

t   Time

$\tau_{1/2}$ Time for 1/2 signal decay

TA   Transient absorption

UV-Vis Ultraviolet-visible

VB   Valence band

V   Volt

W   Watt

λ   Wavelength

XPS X-ray photoelectron spectroscopy

ZrO_2 Zirconium oxide

β   Tunneling decay constant

CHAPTER 1. Enhancing Charge Separation in Dye-Sensitized NiO Photocathodes through Ligand Electronics of Ruthenium Chromophores

Introduction

Dye-sensitized solar cells (DSSCs) and dye-sensitized photoelectrosynthesis cells (DSPECs) provide a promising low-cost technology for capturing and converting solar energy to electricity and fuels, respectively. The vast majority of research in this field has focused on n-type semiconductor materials such as TiO_2.[1] However, the dye-sensitization of p-type semiconductor materials such as NiO has garnered attention as both a new approach to converting solar energy and as a necessary component for tandem configuration devices.[2]

Unfortunately, NiO-based p-type DSSCs typically perform poorly in comparison to TiO_2-based n-type devices.[2] Low power conversion efficiencies of NiO-based systems stem from fast charge recombination kinetics. These high rates of charge recombination have been attributed to the intrinsic electronic properties of NiO, including its low hole mobility, low permittivity and high defect density.[2] In response, scientific interest has quickly grown to understand how materials engineering and chromophore development can be utilized to overcome these issues inherent to NiO and access efficient photocathodes. From a materials perspective, efforts have focused on both improving the preparation of nanostructured, mesoporous NiO electrodes[3,4] and tuning the electronic structure of NiO through morphology control[5] and defect passivation.[6–10] In a

complementary approach, researchers have examined how chromophores can be designed to retard charge recombination.[11–21] For example, "push-pull,"[20,22,23] "donor-sensitizer," and "acceptor-sensitizer" chromophores[17–19,21,24,25] have been designed to localize electrons distal to the surface anchoring moieties in order to enhance charge separation times, which can be quantified by transient absorption measurements. Through these improvements,[17,26] photon conversion efficiencies of 2.51% have been achieved for a p-type DSSC.[27]

While many of the best-performing NiO sensitizers are organic chromophores,[18–20,22,23,25,28–31] ruthenium polypyridyl complexes have also been reported. However, in comparison to the extensive number of ruthenium-based dyes investigated for TiO_2-based photoanodes[1,32–35], the number explored for NiO is few.[12–14,36] Ruthenium-based dyes[11,12,14,37,38] have many properties beneficial to both photoanode and photocathode applications including their long-lived photoexcited state, their chemical stability, and their easy synthetic modification to modulate photophysical and electrochemical properties.[39] Recognizing the utility of ruthenium-based chromophores for the sensitization of NiO, we are interested in better understanding how the ligand electronics of basic ruthenium polypyridyl chromophores influence interfacial charge separation. In the chromophore $[Ru(bpy)_2(dcb)]^{2+}$ (**1**, Scheme 1, bpy = 2,2'-bipyridine, dcb = 4,4'-dicarboxy-2,2'-bipyridine), the carboxylic acid groups of the dcb ligand anchor the dye to the NiO surface.[40] However, the electron-withdrawing nature of the carboxylic acid groups lowers the ligand π* orbitals of the dcb ligand. In the metal-to-ligand charge transfer (MLCT) excited state, an electron localizes on this dcb ligand. Upon hole injection to NiO, this electron remains localized on the ligand proximal to the metal oxide

2

surface.[40] As such, this positioning may facilitate rapid interfacial charge recombination in the charge separated state. We recognized that by incorporating electron-withdrawing groups on the ancillary bipyridine ligands, the MLCT excited state and the electron in the reduced dye is localized distal to the NiO-chromophore interface and have sought to further examine how charge separation timescales are influenced in simple ruthenium polypyridyl complexes (without ancillary acceptor moieties).[11,13,15,40]

In this work, we examine $[Ru(flpy)_2(dcb)]^{2+}$ (**2**, Scheme 1, flpy = 4,4'-bis(trifluoromethyl)-2,2'-bipyridine) in order to understand how simply positioning the ligand with the lowest-energy π^* orbital proximal versus distal to the NiO surface affects both charge recombination dynamics and DSSC performance. Through ultrafast transient absorption studies, we find that indeed the charge separated state can be transiently observed for **2** but not for **1**. In addition, performance of these chromophores in p-type DSSCs reveals improved efficiencies for **2** as compared to **1**, suggesting correlation between elongated recombination time and device efficiency.

Scheme 1.1. Ruthenium complexes investigated in this work.
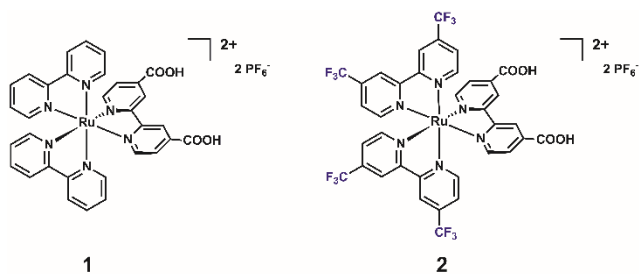
1.1. Experimental methods

1.1.1. General Considerations.

2-Chloro-4-(trifluoromethyl)pyridine, ruthenium trichloride trihydrate (RuCl$_3$·3H$_2$O), 2,2'-bipyridine-4,4'-dicarboxylic acid (dcb) were purchased from Aldrich and used as received. Tetrabutylammonium hexafluorophosphate (TCI, >98%) was recrystallized from hot ethanol, filtered, washed with cold ethanol, and dried under vacuum for 19 h at room temperature before use. All other reagents were ACS grade and used without additional purification. Ru(bpy)$_2$Cl$_2$ was synthesized as previously reported.[41]

1.1.2. Synethesis

4,4'-bis(trifluoromethyl)-2,2'-bipyridine (flpy).

The synthesis of 4,4'-bis(trifluoromethyl)-2,2'-bipyridine (flpy) was accomplished by the nickel catalyzed homo-coupling reaction of 2-chloro-4-(trifluoromethyl)pyridine following a modified literature procedure.[42] Briefly, 2-chloro-4-(trifluoromethyl)pyridine (2 g, 11 mmol), was reacted with NiBr$_2$(PPh$_3$)$_2$ (2.45 g, 3.3 mmol), Zn (1.08 g, 16.5 mmol), and Et$_4$NI (2.83 g, 11 mmol) were refluxed in THF at 60 °C under an inert N$_2$ atmosphere. After the solution was cooled, the mixture was poured into the 10% ammonium hydroxide (100 mL) and extracted with dichloromethane (150 mL x 3 times). The organic layer was dried over MgSO$_4$ and the crude product was purified on silica gel column (10-30% DCM / hexane). White solid was collected. Yield (0.72 g, 22%). ^{1}H NMR (400 MHz, CDCl$_3$): δ 7.57 (2H, d, J=4.8 Hz), 8.72 (2H, s), 8.87 (2H, d, J=4.8 Hz). ^{19}F NMR (377 MHz, CDCl$_3$): δ 64.81.

4,4'-Dimethyl ester-2,2'-bipyridine.

4

4,4'-Dimethyl ester-2,2'-bipyridine (dmeb) was synthesized by a modified literature procedure[43]. 4,4'-Dicarboxy-2,2'-bipyridine (0.13 g, 0.55 mmol), 30 mL of MeOH, and 3 mL of H_2SO_4 were refluxed for 24 hours under N_2. After the solution was cooled, water was added (60 mL) and the solution was basified to pH 8 with a NaOH solution. The product was then extracted with CH_2Cl_2 and the organic layer was dried over $MgSO_4$ and evaporated to yield a white solid.[43] Yield (0.10 g; 67%) ^{1}H NMR (400 MHz, CDCl$_3$): δ 4.03 (6H, s), 7.93 (2H, dd, J=4, 8 Hz), 8.90 (2H, d, J=4Hz), 8.99 (2H, s).

Ru(flpy)$_2$Cl$_2$.

This compound was prepared via modification of the method utilized for Ru(bpy)$_2$Cl$_2$ synthesis.[41] RuCl$_3$·3H$_2$O (0.14 g, 0.7 mmol), flpy (0.40 g, 1.4 mmol), and LiCl (0.17 g, 4.1 mmol) were refluxed in DMF (4 mL) for 8 h under N_2. The reaction mixture was cooled to room temperature, and acetone (32 mL) was added. The reaction mixture was then cooled to 0 °C and vigorously stirred for 1 hour. The solution was then stirred overnight as it warmed to room temperature. The mixture was then filtered over a glass frit, yielding a red-violet filtrate and a black crystalline substance. The solid was washed three times with 10 mL portions of water followed by three 10 mL portions of diethyl ether, and was subsequently dried under vacuum (Yield: 0.18 g; 35%). ^{1}H NMR (400 MHz, DMSO-d$_6$): δ 7.45 (2H, d, J=6.4 Hz), 7.95 (2H, d, J=8 Hz), 8.21 (2H, d, J=6.8 Hz), 9.27 (2H, s), 9.43 (2H, s), 10.19 (2H, d, J=6 Hz)

[Ru(bpy)$_2$(dcb)](PF$_6$)$_2$ (1).

[Ru(bpy)$_2$(dcb)](PF$_6$)$_2$ was prepared with modified literature procedure.[43] Ru(bpy)$_2$Cl$_2$ (0.60 g, 1.2 mmol) and 4,4'-dicarboxy-2,2'-bipyridine (0.30 g, 1.2 mmol) were combined

and heated to refluxed in 1:1 (v/v) EtOH:H$_2$O (50 mL) under N$_2$ condition for 12 hours. After the mixture was cooled to the room temperature, excess NH$_4$PF$_6$ was added, and the solvent was removed by rotary evaporation. The crude solid was washed with distilled water and ether to yield 0.91 g of orange solid powder. (Yield: 78%) ^{1}H NMR (400 MHz, DMSO-d$_6$): δ 7.53 (4H, dt, J=6, 22 Hz), 7.73 (4H, dd, J=4.8, 16 Hz), 7.90 (4H, dd, J=5.6, 26 Hz), 8.19 (4H, m), 8.85 (4H, m), 9.24 (2H, s).

[Ru(bpy)$_2$(dmeb)](PF$_6$)$_2$ (1′).

This compound was prepared through a method similar to that employed for **1**, using dmeb ligand as an auxiliary ligand. A mixture of Ru(bpy)$_2$Cl$_2$ (0.12 g, 0.26 mmol) and dmeb (0.07 g, 0.26 mmol) in 1:1 (v/v) EtOH:H$_2$O (20 mL) was heated to reflux under N$_2$ for 12 hours. After the solution was cooled to the room temperature, excess NH$_4$PF$_6$ was added and the solvent was removed by rotary evaporation. The crude solid was washed with distilled water and ether and filtrated to yield 0.02 g of orange solid powder was collected.[43] (Yield: 85%) ^{1}H NMR (400 MHz, DMSO-d$_6$): δ 3.42 (6H, s), 6.94 (2H, t, J=4 Hz), 7.01 (2H, t, J=4 Hz), 7.16 (4H, m), 7.34 (2H, dd, J=4, 8 Hz), 7.43 (2H, d, J=4 Hz), 7.64 (4H, m), 8.30 (4H, m), 8.78 (2H, s)

[Ru(flpy)$_2$(dcb)](PF$_6$)$_2$ (2).

This compound was synthesized by a modified literature procedure.[43] Ru(flpy)$_2$Cl$_2$ (0.15 g, 0.21 mmol) and 2,2'-bipyridine-4,4'-dicarboxylic acid (0.05 g, 0.21 mmol) were combined and heated to reflux in 1:1 (v/v) EtOH:H$_2$O (20 mL) under a N$_2$ atmosphere for three days. The reaction mixture was cooled to room temperature and excess NH$_4$PF$_6$ was added to precipitate the product. Subsequently, solvent was removed with rotary

evaporation. The crude solid was washed with distilled water and ether and filtered. 0.02 g orange-red solid powder was collected. (Yield: 82%) ^{1}H NMR (400 MHz, DMSO-d$_6$): δ 7.80 (2H, d, J=4.8 Hz), 7.85 (4H, m), 7.89(2H, d, 5.2 Hz), 7.99 (2H, d, J=6Hz), 8.09 (2H, d, J=5.6 Hz), 9.17 (2H, s), 9.56 (4H, s). ^{19}F NMR (377 MHz, CDCl$_3$): δ -71.1 (s, 6F), -69.2 (s, 6F).

1.1.3. Absorbance and Steady-State Emission.

Absorbance measurements were acquired with an Agilent Cary 60 UV-Vis absorption spectrometer (for solution measurements) and a Cary 5000 UV-Vis Spectrometer with integrating sphere attachment (for the film samples). Room temperature emission spectra were collected with a QuantaMaster QM4SE emission spectrometer from Photon Technology International. Low temperature emission spectra were collected with an Edinburgh Instruments FLS920 spectrometer, with excitation by an Edinburgh EPL-445 ps pulsed laser diode (444.2 nm, pulse width = 95 ps, 2 MHz). All spectra were corrected for fluctuations in lamp intensity and the spectral response of the monochromator and photomultiplier tube.

For film measurements, films were inserted diagonally into a 10 mm path length quartz cuvette whose top had been adapted with a no. 15 O-ring sealing joint, side arm, and Kontes valve. The cuvette was filled with a 0.1 M LiClO$_4$ CH$_3$CN solution and the sample was sparged with N$_2$ for 40 min prior to recording absorbance or emission data. All solution samples were prepared under an inert atmosphere and recorded in 10 mm pathlength, air-tight quartz cuvettes.

1.1.4. Electrochemical Measurements.

Cyclic voltammograms were collected in a nitrogen-filled glovebox with a Pine Instruments WaveDriver potentiostat using glassy carbon working electrodes, a platinum counter electrode, and a $Ag/AgNO_3$ (10 mM $AgNO_3$) reference electrode. All scans were performed in acetonitrile solutions with 200 mM $[Bu_4N][PF_6]$ and referenced to the ferrocene/ferrocenium couple ($Fc^{+/0}$). Glassy carbon working electrodes (CH Instruments, 3 mm diameter) were polished with 0.3 micron alumina powder and 0.05 micron alumina powder (CH Instruments, contained no agglomerating agents), rinsed and ultrasonicated for one minute in HPLC grade water to remove residual polishing powder.

1.1.5. Metal Oxide Film Fabrication.

FTO glass substrates (fluorine doped SnO_2, Hartford Glass, Inc., TEC 15) were cut to size and then cleaned in an ultrasonic bath first in acetone and finally in ethanol, for 30 minutes each. Nanocrystalline ZrO_2 films were prepared on FTO-coated glass according to a previously reported procedure.[44] Thin films were prepared using the doctor blade method with tape-casting and sintered at 450 °C for 120 min. All films were approximately 1.4 μM thick. Nanocrystalline NiO films were prepared using a sol-gel method. A 1 wt% suspension of hydroxypropyl cellulose (HPC) in ethanol was prepared by adding 1.3 g HPC to 15 mL ethanol followed by stirring overnight. 0.5g Ni-Nanoxide N/SP nanoparticle paste (Solaronix) was transferred to 5 ml ethanol and sonicated for 20 minutes followed by ultrasonication for 5 minutes with a sonicating horn. To this freshly mixed NiO dispersion, 5mL of the 10 wt% HPC suspension were added and the final mixture stirred overnight. NiO films were deposited onto conducting glass substrates by the doctor blade technique. Film thickness was controlled by the numbered layers of

scotch tape used for define the exposed area. For thermal annealing, the NiO films were placed in a Thermo Scientific TM box furnace. The temperature was ramped to 400 °C in 30 min, held for 1 hour at 400 °C; and lowered back to room temperature for 1 hour in air. The obtained film thickness after annealing was approximately 1.2 μm, when one layer of scotch tape was used. A Dektak Bruker profilometer was used to determine film thickness. Preparation of mesoporous electrodes with NiO nanoplatelets are described below in the DSSC Preparation section.

1.1.6. Surface Loading of Dyes on NiO and ZrO$_2$ Films.

For optical characterization (absorbance, transient absorption, spectroelectrochemistry), nanocrystalline films were loaded with chromophores to produce chromophore-derivatized films. Sensitizers were anchored to the NiO and ZrO$_2$ nanocrystalline films by immersing the sintered slides overnight in methanol solutions containing compound **1** or **2** (1×10^{-5} - 2×10^{-5} M). The slides were then soaked in methanol solution to remove excess unanchored complexes. Surface loading was quantified via UV-Vis absorption spectroscopy per previously reported methods,[45,46] where Γ (mol cm^{-2}) = A(λ)/ε(λ)/1000, using the molar extinction coefficients (ε) in solution. The extent of surface loading coverage of the nanocrystalline films is estimated as Γ = 4.9×10^{-9} mol cm^{-2} and Γ = 6.13×10^{-9} mol cm^{-2} respectively for **1** and **2**.

1.1.7. Nanosecond Transient Absorption Spectroscopy.

All samples utilized in transient absorption measurements were were prepared in 0.1 M LiClO$_4$ CH$_3$CN solution under an inert atmosphere and recorded in 10 mm pathlength, air-tight quartz cuvettes. Samples were purged with N$_2$ for at least 40 min prior to

experimentation. Transient absorption experiments were performed using a custom-built laser flash photolysis system. Laser excitation (5-7 ns FWHM, 10 Hz, Q-switched) was provided by the third harmonic of a Nd:YAG laser (Spectra-Physics, Inc., model Quanta-Ray LAB-170-10) that pumped an OPO (basiScan, GWU Lasertechnik) to access tunable excitation (415–800 nm). Laser power at the sample cuvette was attenuated by the use of a half waveplate (WPMH10M-355, ThorLabs) and polarizer (GL10-A, ThorLabs). A glass window was used to deflect a small portion of excitation beam to a Si diode detector (DET10A, ThorLabs), triggering the oscilloscope to start data collection. Timing of the laser was controlled by a digital delay generator (9514+ Pulse Generator, Quantum Composers).

A 75 watt Xe Arc Lamp (PowerArc, Optical Building Blocks) was used in continuous wave mode as a white light source. The probe beam was passed through a 375 nm long pass filter before passing through the sample collinear with the pump beam. Probe light was then attenuated using a neutral density filter, and scatted excitation light is filtered with a color filter wheel containing various long pass and short pass filters. Single wavelength kinetics were obtained using a double slit monochomator (Spectral Products CM112) outfitted with a Hamamatsu R928 photomultiplier tube (PMT). The signal was amplified by a 200 MHz wideband voltage amplifier (DHPVA-200, Electro Optical Components), and processed using a digitizer (CompuScope 12502, GaGeScope) controlled by custom software (MATLAB). The data were converted to units of ΔOD (ΔOD = -log(I/I_0), where I is the time-resolved probe light intensity with laser excitation, and I_0 is the intensity without excitation). Data was further analyzed in Igor Pro 6.22 (Wavemetrics).

1.1.8. Ultrafast Transient Absorption Spectroscopy.

Ultrafast transient absorption was performed using a 1 kHz regeneratively amplified Ti:Sapphire laser system, Clark-MXR CPA2210. A portion of the 775 nm laser fundamental was converted to 1834 nm via optical parametric amplification. This beam was then frequency doubled to 917 nm with a BBO crystal, and then combined with residual 775 nm in another BBO crystal to yield the 420 nm pump. The white light continuum probe was generated by pumping a translating CaF_2 plate with another portion of the 775 nm laser fundamental. The polarization of the pump was set to the magic angle, 54.7°, relative to the white light continuum probe with a waveplate. Timing of the pump and probe was achieved with a computer controlled delay stage. Low pass filters were employed on the pump and probe to eliminate residual 775 nm fundamental. The per-pulse fluence was 450 $\mu J/cm^2$ or less. Data collection and analysis was performed with custom made LabView software. Optical chirp was corrected according to the frequency resolved optical gating of a glass slide.

1.1.9. DSSC Preparation.

p-type dye-sensitized solar cells were fabricated as previously described.[5,6] Mesoporous electrodes (~1.6 μm in thickness) of NiO nanoplatelets were obtained by spincasting (Laurell WS-650MZ-23NPP) a viscous nanoparticle paste onto fluorine-doped tin oxide (FTO glass; Hartford Glass, TEC15).[47] The films were then annealed (450 °C, 40 min; <20% Humidity). The active area of the electrodes was defined by mechanically removing excess material. The electrodes were then immersed in dye solution (0.1 mM in EtOH) overnight, rinsed with IPA, and dried with N_2. Thermal decomposition (380 °C,

30 min) of chloroplatinic acid (5 mM in IPA) was performed on FTO glass with a pre-drilled hole to fabricate the counter electrode. The electrodes were then sandwiched using a 25 μm Surlyn gasket in a custom-made heat press (150 °C; 10 s). The hole was sealed with Surlyn (150 °C; 5 s). Z960-like electrolyte (1.0 M 1,3-dimethylimidazolium iodide, iodide (0.03 M), tert-butylpyridine (0.5 M), and guanidium thiocynanate (0.1 M) in 85/15 (v/v) acetonitrile/valeronitrile) was vacuum backfilled. The cell was then sealed (150 °C; 5 s) with a Surlyn film and a microscope coverslip.

1.1.10. DSSC Characterization.

Light harvesting efficiencies (LHE) were calculated by subtracting the absorbance of the undyed films from the dyed films with a systematic offset at 700 nm to account for small variability in background absorption. The difference spectra was then converted to absorptance. The LHE values presented here thus represent dye only.

J-V curves were obtained using a Newport Oriel 150W class ABB AM1.5G solar simulator calibrated to 1-sun intensity with a certified reference solar cell (Newport 91150V) using a Keithley 2636A sourcemeter. Incident photon to current efficiency (IPCE) measurements were obtained by illuminating devices with a tungsten lamp (Newport Instruments) coupled to a spectrometer (Princeton Instruments SP-2300). Device carrier lifetimes were obtained from *Voc* decays (sampling rate, 1 kHz) with a starting illumination of 1-sun and a shutter response of <1 s. The decay was fit to a tri-exponential decay with an adjusted-R^2>0.98. The derivative of the decay, $\left[\frac{dV_{oc}}{dt}\right]$, was input into Equation 1:

$$Lifetime = \frac{kT}{q} \cdot \left[\frac{dV_{oc}}{dt}\right]^{-1} \qquad \text{Eq. 1}$$

where k is the Boltzmann constant, T is temperature, and q is the elementary charge.

1.2. Results and Discussions

1.2.1. Synthesis and Characterization of Chromophores.

1 and **2** were synthesized following modified literature procedures (Scheme 2). Briefly, the flpy ligand was synthesized via a Negishi coupling of 2-chloro-4-trifluoromethyl)pyridine.[42] Ru(flpy)$_2$Cl$_2$ and Ru(bpy)$_2$Cl$_2$ were prepared by refluxing RuCl$_3$·H$_2$O with two equivalents of the corresponding bipyridine in N,N-dimethylformamide in the presence of LiCl.[48] The heteroleptic ruthenium complexes **1** and **2** were obtained via reaction of Ru(bpy)$_2$Cl$_2$ and Ru(flpy)$_2$Cl$_2$ with 4,4'-dicarboxy-2,2'-bipyridine, followed by anion exchange with NH$_4$PF$_6$.
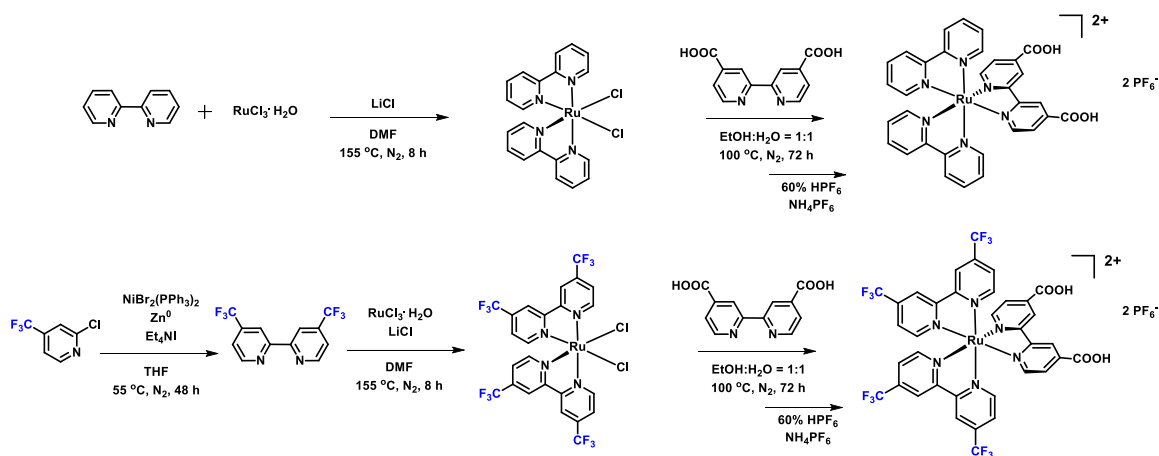
Scheme 1.2. Synthesis of **1** and **2**.

Both **1** and **2** exhibit similar absorbance features in acetonitrile (Figure 1). In the UV region, intense ligand-localized $\pi \rightarrow \pi^*$ charge transfer transitions are observed below 300 nm. Broad metal-to-ligand (MLCT) absorption bands[39] are observed centered at 468 (**1**) and 460 (**2**) nm, with molar extinction coefficients measured as 13,750 (**1**) and 12,630 (**2**) $M^{-1}cm^{-1}$, consistent with previous reports.[49] Upon excitation, both complexes display structureless luminescence centered at 642 (**1**) and 674 (**2**) nm at room temperature (Figure 1). The free energy stored in the excited state (ΔG_{ES}) was estimated from a tangent line drawn on the high-energy vibronic progression in corrected PL spectrum at low temperature, following a previously reported procedure (Table 1)[50]

Table 1.1. Photophysical and electrochemical data of compound **1** and **2**

Dye	λ_{abs} (nm)	λ_{em} (nm)	$E^{\circ\prime}_{ox}$ [§]	$E^{\circ\prime}_{red}$ [§]	ΔG_{es} (eV)	$E^{\circ\prime *}$ [§]
1	468	642	1.00	-1.70, -1.92, -2.23	2.11	0.41
2	460	674	1.28	-1.24, -1.43, -2.05	2.16	0.92

§ V vs. $Fc^{+/0}$
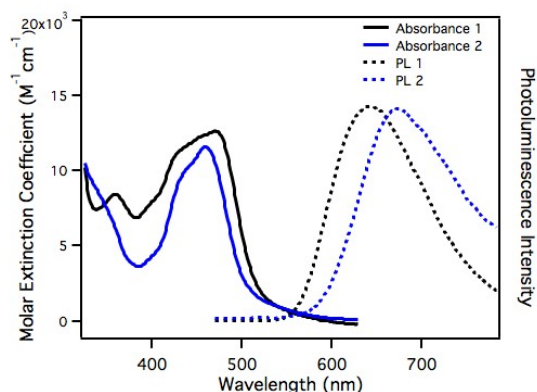
Figure 1.1. Normalized absorption and photoluminescence spectra of **1** and **2** in acetonitrile solutions.

Nanosecond transient absorption (TA) spectroscopy was carried out to investigate the excited state of ruthenium dyes in acetonitrile (Figure 2). Upon excitation, the TA spectra of both sensitizers display a ground-state bleach centered around 450 nm, which roughly mirrors the ground-state absorption peak. A positive absorption band at 385 nm is assigned to a $\pi \rightarrow \pi^*$ transient feature. The decay of these excited-state features (Figure 3) were fit to single exponential functions ($\tau(\mathbf{1}) = 0.88$ μs, $\tau(\mathbf{2}) = 1.12$ μs); the excited state lifetimes are in good agreement with the time-resolved photoluminescence lifetimes ($\tau(\mathbf{1}) = 0.89$ μs, $\tau(\mathbf{2}) = 1.19$ μs).
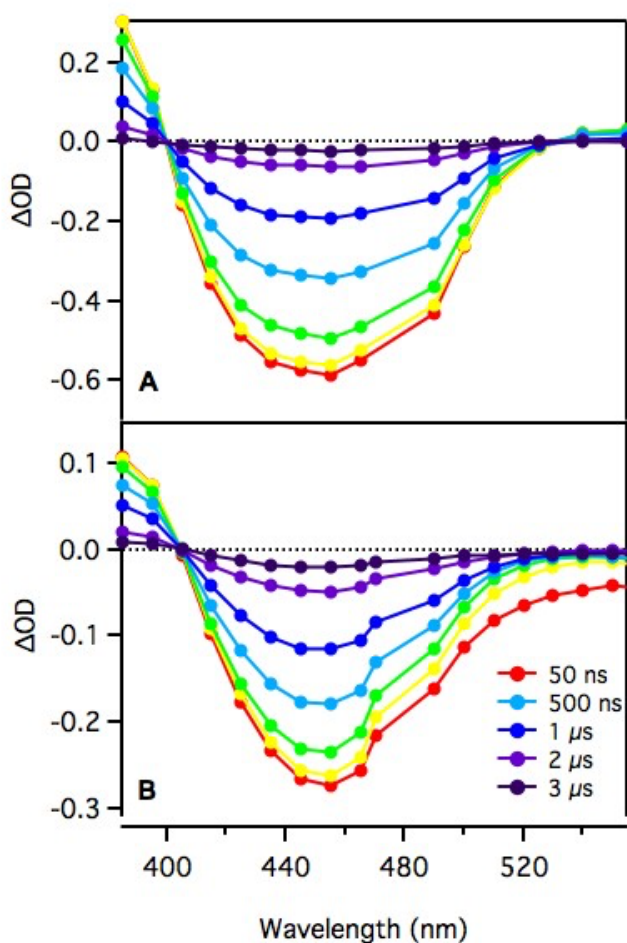
Figure 1.2. Transient absorption spectra of (A) **1** and (B) **2** in 0.1 M LiClO$_4$ CH$_3$CN solution at various time delays. $\lambda_{\text{ex}} = 480$ nm, 3.8 mJ/pulse.
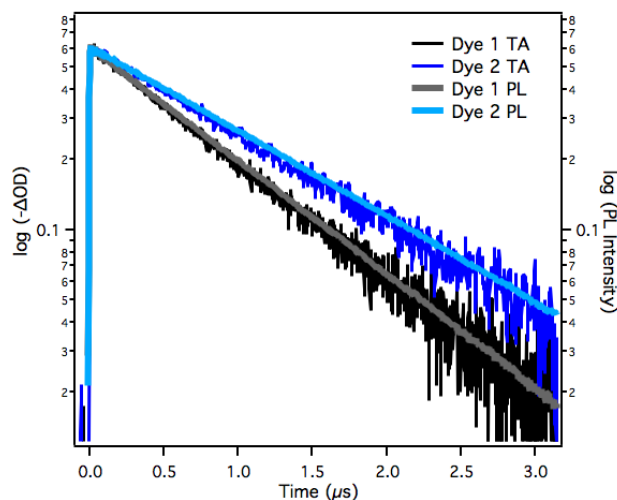
Figure 1.3. Transient absorption kinetics traces and time-resolved emission decay of **1** and **2** in degassed CH_3CN solutions. Transient absorption: λ_{ex} = 480 nm, λ_{obs} = 445 nm, $\tau(\mathbf{1})$ = 0.88 μs, $\tau(\mathbf{2})$ = 1.12 μs. . Emission: λ_{ex} = 480 nm, λ_{obs} = 650 nm, $\tau(\mathbf{1})$ = 0.89 μs, $\tau(\mathbf{2})$ = 1.19 μs.

Cyclic voltammograms of **1** and **2** in acetonitrile solution both show a reversible oxidation feature (1.00 and 1.28 V vs $Fc^{0/+}$, respectively), assigned to the Ru(III/II) couple (Figure 4). The 280 mV difference in these potentials is consistent with the electron-withdrawing nature of the flpy ligands, which makes the ruthenium center of **2** harder to oxidize. Three ligand-based reductions are observed in the cathodic scans. Two quasi-reversible peaks at −1.24 and −1.43 V vs. $Fc^{+/0}$ and an irreversible peak at −2.05 V vs $Fc^{+/0}$ are observed for **2**. For comparison, $[Ru(flpy)_2(bpy)]^{2+}$ exhibits ligand based reductions at −1.21, −1.40 and −1.89 V vs. $Fc^{+/0}$ which correspond to the reduction of two flpy ligands, followed by reduction of the bpy ligand.[51] The similarity between the first two reduction potentials of **2** and $[Ru(flpy)_2(bpy)]^{2+}$ supports assignment of the flpy

16

ligands as the most readily reduced ligands on **2**, and suggests the lowest-lying MLCT excited state will indeed localize the electron in the π* orbital of a flpy ligand. **1** has an irreversible reduction peak at −1.70 V, assigned to the dcb ligand, and quasi-reversible peaks at −1.92 and −2.23 V, assigned two bpy ligands, respectively. Other ruthenium complexes featuring dicarboxylic acid bipyridine ligands have also been reported to have quasi and irreversible ligand-based reductions, attributed to hydrogen gas generation by electrochemically induced deprotonation of the linkage.[52,53] These ligand based reduction assignments indicate that, in contrast to **2**, the lowest-lying MLCT excited state of **1** will localize the electron in the π* orbital of the dcb ligand.
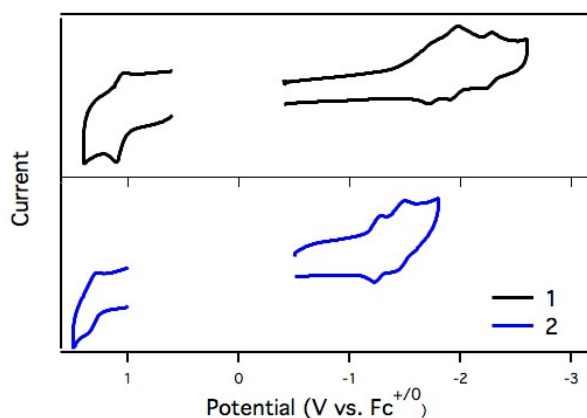
Figure 1.4. Cyclic voltammograms of compound **1** and **2** recorded at 100 mV/s in a 200 mM [Bu$_4$N][PF$_6$] CH$_3$CN solution.

The excited-state reduction potentials of **1** and **2** were estimated from the ground state reduction potentials and the free energy stored in the excited state, per Eq. 2.[54]

$$E^{\circ\prime}(Ru^{2+*}/Ru^{2+}L^{\bullet-}) = E^{\circ\prime}(Ru^{2+}/Ru^{2+}L^{\bullet-}) - \Delta G_{ES} \text{ Eq. 2}$$

2 is a stronger excited-state oxidant ($E^{\circ\prime}(\mathbf{2}^{*/-})$ = 0.92 V vs. Fc$^{+/0}$) in comparison to **1** ($E^{\circ\prime}(\mathbf{1}^{*/-})$ = 0.41 V vs. Fc$^{+/0}$), but both species are capable of hole injection to the valence band of NiO (0.54 V vs. NHE at pH 7, approximately 0.16 V vs Fc$^{+/0}$).[55]

In order to determine the spectroscopic signatures of the reduced chromophores, **1** and

2 were irradiated with a blue LED ($\lambda = 460$ nm) in the presence of a sacrificial reductant,

triethylamine (TEA, $E^{\circ\prime}(\text{TEA}^{+/0}) = 0.40$ V vs. $\text{Fc}^{+/0}$).[22] Upon irradiation of **2** under these

conditions, the absorbance red-shifted ($\lambda_{max} = 522$ nm), consistent with the reduction to

the corresponding reduced species, **2**$^{-}$ (Figure 5A).[58] By contrast, photolysis of **1** simply

led to a bleach, and slight blue shift, of the MLCT absorbance feature (Figure 5B).

However, stability of **1** was improved upon esterification of the carboxylic acid groups to

form **1′**. Photolysis of **1′** in the presence of TEA generated the reduced ruthenium species

1′$^{-}$ ($\lambda_{max} = 492$ nm, Figure 5C), consistent with previous reports.[58] Because of the similar

optical properties of **1** and **1′**, the absorbance spectrum of **1**$^{-}$ is assumed to be nearly

identical to that obtained for **1′**$^{-}$.
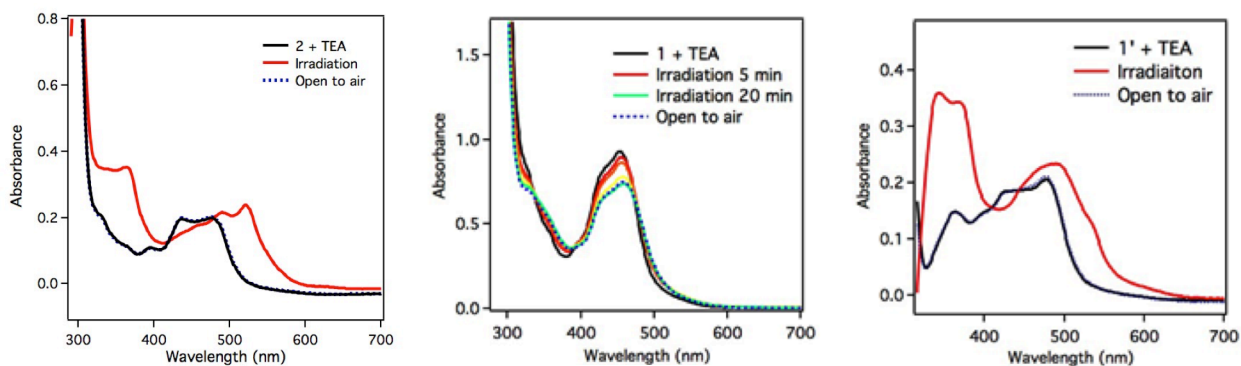
Figure 1.5. Absorption spectra of (left) **2**, (center) **1** and (right) **1′** in CH$_3$CN in the

presence of 0.1 M TEA, before irradiation (black lines); after irradiation with blue LED

(red lines); and after exposure to air to reoxidize the reduced species (dotted lines)

1.2.2. Sensitization of NiO.

Nanocrystalline NiO films were sensitized with solutions of **1** and **2** in ethanol. To quantify dye loading on NiO films, absorbance spectra of dye-sensitized NiO film were recorded using an integrating sphere (Figure 6); coverages were estimated at 4.9 nmol/cm^2 and 6.13 nmol/cm^2 respectively for **1** and **2**, which indicates loading of the nanocrystalline is more effective based than the monolayer coverage value for a flat surface (ca. 1×10^{-10} mol/cm^2).[46] The absorbance of **1** and **2** adsorbed on the NiO surface was determined by taking the difference between the sensitized and un-sensitized films. The spectral profiles of **1**-NiO and **2**-NiO were very similar to solutions of **1** and **2**, indicating surface anchoring does not lead to ground-state dye aggregation.
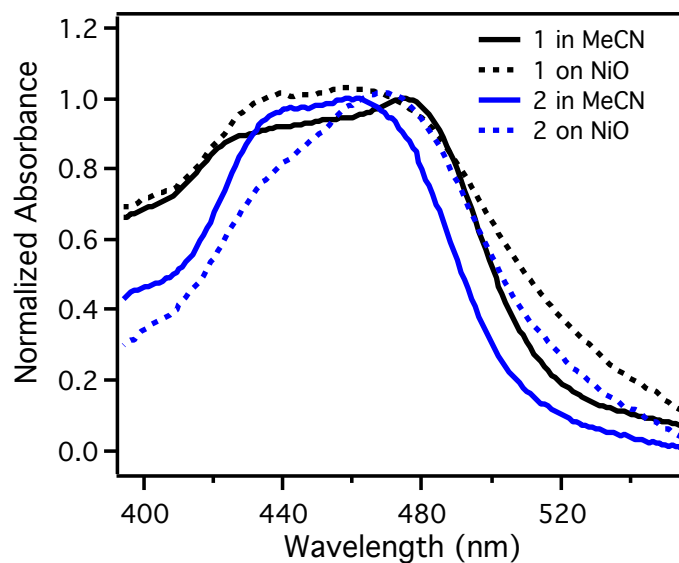
Figure 1.6. Normalized absorbance spectra of **1** and **2** in CH$_3$CN solution (solid) and on NiO (dashed). The NiO sample was measured with an integrating sphere attachment and the NiO background was subtracted.

Photoluminescence spectra were obtained for **1-NiO** and **2-NiO**, along with **1-ZrO$_2$** and **2-ZrO$_2$**. The valence band of of ZrO$_2$ is approximately 4.0 V (vs. NHE at pH 0,

approximately 3.37 V vs Fc$^{0/+}$), which is more positive than the excited state reduction potential of ruthenium dyes; therefore, hole injection from excited dye is thermodynamically unfavorable.[59] For the ZrO$_2$-anchored chromophores, photoluminescence spectra similar to the solution samples of **1** and **2** are obtained (λ_{max} = 650 and 665 nm, respectively). By contrast, the photoluminescence intensity of the NiO-anchored chromophores is quenched (Figure 7). This significant emission quenching is attributed to ultrafast hole injection into NiO for both **1** and **2**, though non-radiative decay processes could also be contributing.
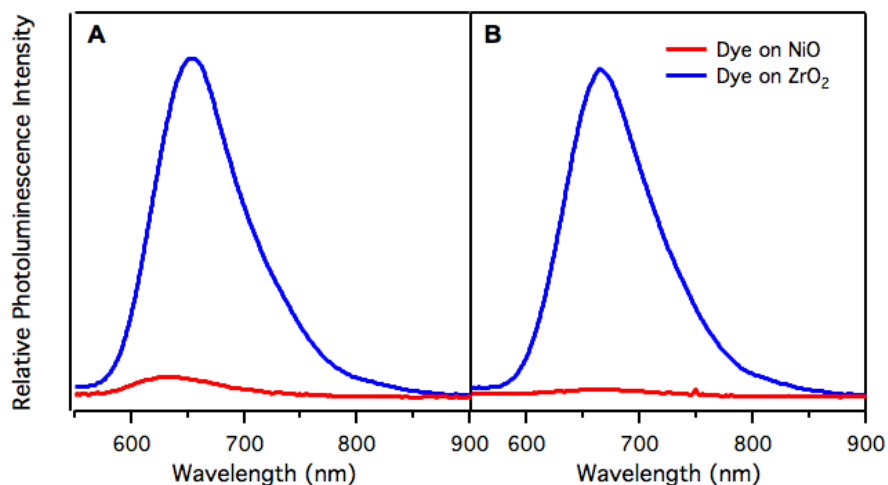
Figure 1.7. Photoluminescence spectra of (A) **1** and (B) **2** anchored on ZrO$_2$(blue) and NiO (red) mesoporous thin films in N$_2$ purged acetonitrile (λ_{ex} = 420 nm).

1.2.3. Interfacial Charge Separation.

Ultrafast TA experiments were performed on sensitized NiO and ZrO$_2$ films. Upon excitation (λ_{ex} = 420 nm), the transient difference spectra of **2-ZrO$_2$** (Figure 8) is dominated by a bleach of the ^{3}MLCT absorption centered at 460 nm and a $\pi \rightarrow \pi^*$ absorbance centered at 376 nm, consistent with the excited-state transient spectra

recorded for **2** in solution (see above) and the [3]MLCT excited state of other polypyridyl ruthenium complexes.[60] For **1-NiO** and **2-NiO**, the transient difference spectra recorded at 3 ps both exhibit similar features to the ZrO_2-sensitized film (Figure 9), consistent with initial formation of the [3]MLCT excited states of **1** and **2**. For **1-NiO** and **2-NiO**, the excited state transient features decay rapidly on the sub-nanosecond timescale. The kinetics for the recovery of the ground state bleach at 464 nm are shown in Figure 10; traces for biexponential decays (dashed lines) consisting of fast 10's of ps decay and a 2 ns slow decay are included to guide the reader. These data are consistent with hole injection to form the charge separated state $(Ru^{2+}L^{\bullet-}–NiO(h^+))$ followed by rapid charge recombination, as has been observed for similar chromophores on NiO.[21,23,61]
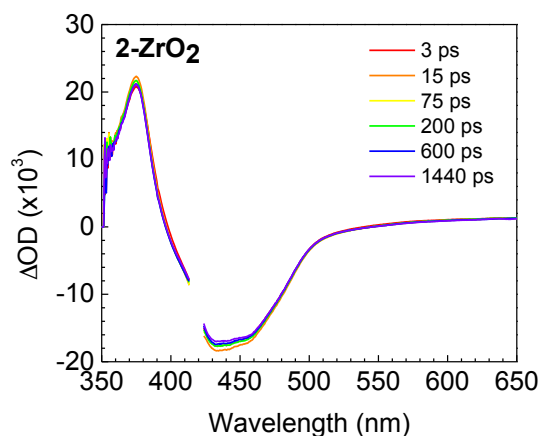
Figure 1.8. Transient absorption spectra for **2-ZrO₂** in 0.1 M $LiClO_4$ containing CH_3CN. $\lambda_{ex} = 420$ nm, 140 nJ/pulse.

For **2-NiO**, a small but distinct absorbance feature centered at 525 nm grows in over the first hundred picoseconds (Figure 9), consistent with the transient formation of **2**⁻ (see above). The small quantity of **2**⁻ formed does not decay on the picosecond timescale. The observed slow decay at 525 nm in the kinetics traces is observed across the whole

spectrum (and in **1-NiO**) and is likely due to the NiO becoming less reflective or more transparent following heating the laser pulse. For kinetics at 525 nm for **1-NiO** (Figure 10), a single exponential 350 ps decay with an offset is used to describe the increased transmittance from sample heating. Since the magnitude of the heating artifact appears to be similar for both samples, the 525 nm kinetics for **2-NiO** are described with a biexponential guide line consisting of a 37 ps growth corresponding to the production of reduced dye, and the 350 ps decay observed for heating in **1-NiO**.

The observation of the $Ru^{2+}L^{\bullet-}–NiO(h^+)$ charge separated state for **2-NiO** but not **1-NiO** indicates that the electronic structure of the ruthenium chromophore can enhance charge separation timescales. Specifically, these data suggest that the electron-withdrawing flpy ligand of **2** promotes localization of the electron in the charge separated state on the bipyridine distal to the NiO surface as opposed to the proximal dcb ligand. This increased charge separation distance attenuates recombination kinetics.
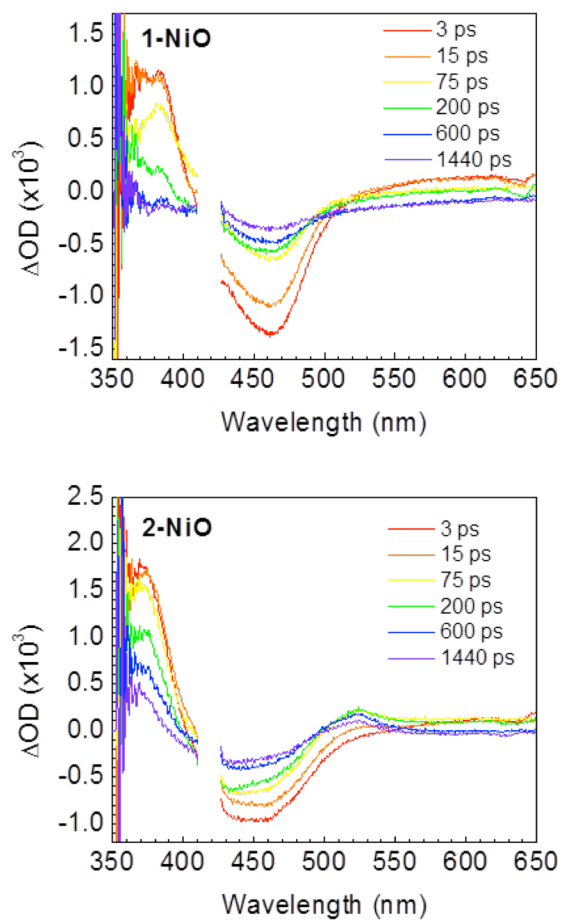
Figure 1.9. Transient absorption spectra for **1-NiO** (top) and **2-NiO** (bottom) in 0.1 M LiClO$_4$ CH$_3$CN solution. λ_{ex} = 420 nm, 140 nJ/pulse.
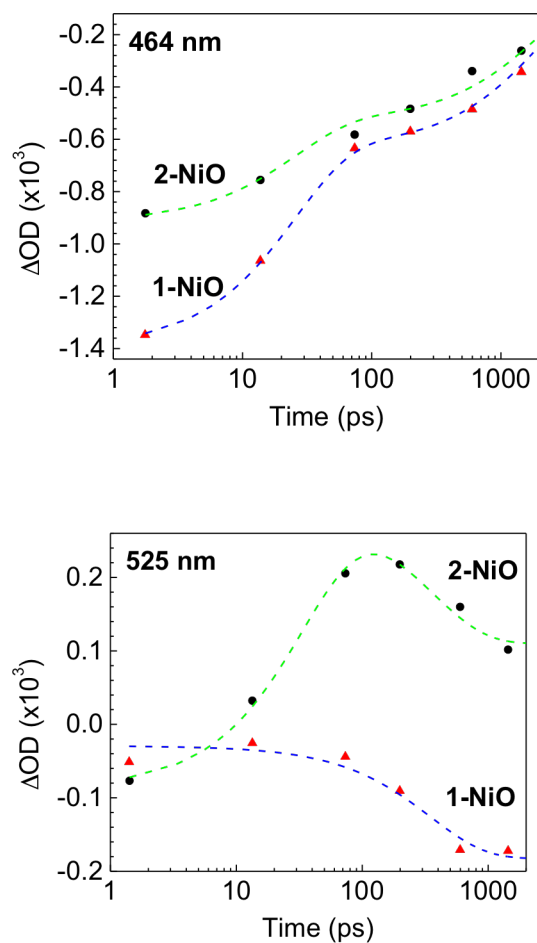
Figure 1.10. Single wavelength kinetics for of **1-NiO** and **2-NiO** at 464 nm (top) and 525 nm (bottom). Dashed lines are provided as a guide to the eye. λ_{ex} = 420 nm, 140 nJ/pulse.

Table 1.2. Parameters for kinetics modeling in Figure 10.

	A1 (mOD)	t1 (ps)	A2 (mOD)	t2 (ps)	y0 (mOD)
464 nm					
1-NiO	-0.79	25	-0.62	2470	0
2-NiO	-0.37	47	-0.51	1930	0
525 nm					
1-NiO	0.153	350	-	-	-0.183
2-NiO	-0.389	37.4	0.193	350	0.110

1.2.4. Device Performance.

NiO nanoplatelets[5] were utilized for the investigation of photovoltaic performances of compounds **1** and **2** as well as a commonly utilized chromophore Coumarin 343 (C343). For DSSC devices, this material has shown advantageous properties such as high surface area and 10-fold higher electrical mobilities over conventional nanoparticle NiO thin film.[5] As such, we utilized this material, as opposed to the sol-gel NiO films utilized for spectroscopic studies, when analyzing the device performance. The J-V curves (Figure 11A, Table 3) for the devices show the open-circuit voltages of the devices appear to be nearly identical for the three dyes but a significantly enhanced (57% relative increase) photocurrent density is observed for **2** (Table 3). Differences in charge-carrier lifetimes in devices (Figure 11B, Table 3) were also explored by open-circuit voltage decays, and showed a negligible change between **1** and **2**. The overall device efficiency of **2** increased by 73% relative to **1**, which is primarily due to the large increase in J_{sc}. The origin of the photocurrent was confirmed to primarily come from the chromophore absorption by incident photon-to-current conversion efficiencies (Figure 9C, Table 3). Additionally, there is a large difference in the amount of light absorbed by each chromophore. The dye-only light-harvesting efficiencies at the λ_{max} are ~91, 38, 22 % for C343, **1**, and **2** respectively. From these data, the large increase in current for the chromophore **2** (which has the lowest LHE) represents a significant increase in the internal quantum efficiency either through an increase in injection efficiency or the charge collection efficiency.
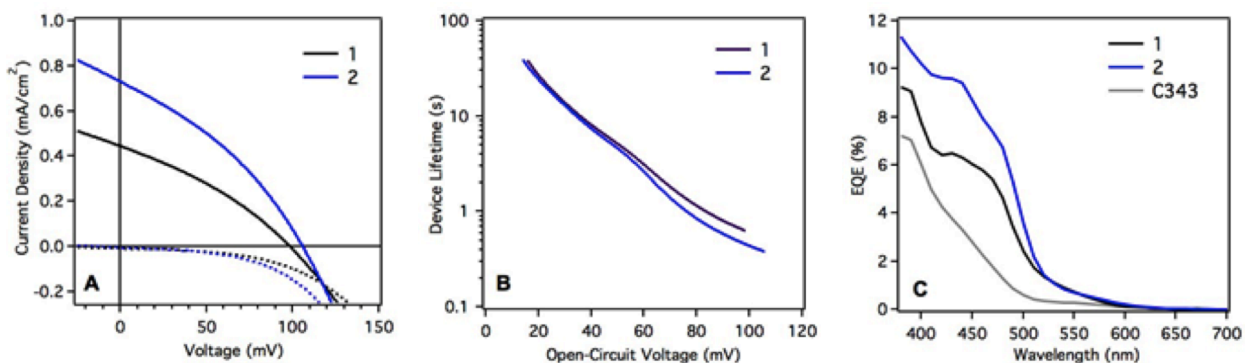
Figure 1.11. Photovoltaic performance of p-type DSSC devices with **1** and **2**. (A) Current density – voltage curves under simulated 1-sun illumination (colored lines) and in the dark (dashed lines) for p-DSSC devices utilizing dyes **1** and **2**. (B) Device carrier lifetimes as determined from open-circuit voltage decay experiments for dyes **1** and **2** decaying from simulating 1-sun illumination to dark with a sampling rate of 1kHz. (C) External quantum efficiency – wavelength curves for dyes **1** and **2**. Data for the C343 dyes included in Panel C for comparison; additional C343 data for comparison is included in Table 3.

Table 1.3. Photovoltaic metrics (n≥4) for NiO DSSC devices using the C343, **1**, and **2** chromophores

	V_{OC} (mV)	J_{SC} (mA/cm^2)	FF (%)	η (%)	λ_{max} (nm)	*LHE* λ_{max} *(%)*	*EQE* λ_{max} *(%)*	*IQE* λ_{max} *(%)*
C343	105 ± 3	0.49 ± 0.06	32.4 ± 0.7	0.017 ± 0.002	410	91.3	5.0	5.5
1	101 ± 2	0.47 ± 0.08	32.0 ± 1	0.015 ± 0.003	460	38.2	5.8	15.2
2	104 ± 3	0.74 ± 0.04	33.9 ± 0.3	0.0260 ± 0.0009	460	21.6	8.0	36.9

1.3. Conclusions

We have demonstrated that the interfacial charge separation dynamics of ruthenium polypyridyl-sensitized NiO are influenced by the electronic structure of the chromophore. Ultrafast transient absorption experiments reveal distinctly different excited-state dynamics for **1-NiO** and **2-NiO**. For **1-NiO**, no charge separated state is observed, but rather the transient features associated with the chromophore excited-state decay rapidly, consistent with rapid charge recombination upon hole injection. By contrast, a charge separated state is observed for **2-NiO**, as evidenced by a transient feature ($\lambda_{max} = 525$ nm) consistent with the reduced chromophore **2$^-$**. The differences observed between the two chromophores are attributed to electron withdrawing $-CF_3$ functional groups on the ancillary ligands of **2**. This lowers the π^* orbital of the ancillary ligand below that of the surface-anchoring dcb ligand, positioning the bipyridine radical distal from the surface in the charge-separated state of **2-NiO**. By contrast, in **1$^-$** the electron is localized on the dcb ligand, proximal to the NiO surface. The observation of elongated charge separation for

2-NiO vs. **1-NiO** correlates with an enhanced photovoltaic performance observed for NiO DSSC devices prepared with **2** vs. **1**. These data provide a simple yet promising molecular design strategy for enhancing efficiency in NiO DSSCs.

Chapter 2. Charge Recombination Dynamics in Dye-Sensitized SnO$_2$/TiO$_2$ Core/Shell Architectures

Introduction

In the search for successful strategies for dye-sensitized solar cells (DSSCs) and dye-sensitized photoelectrosynthesis cells (DSPECs), one approach to achieving structural control of electron transfer dynamics at the oxide interface in devices is implementation of core/shell metal oxide electrode structures. [62,63] Enhanced efficiencies in core/shell architecture come from the staggered band energy position (Scheme 1-a), where the conduction band potential of the shell is more negative than that of the core. Such unique structure comes to a key to inhibit detrimental back electron transfer as the shell acts as a significant barrier for BET from electron localized in core conduction band. Thus, application of the core/shell structure has led to a greatly enhanced efficiencies for visible-light-driven water oxidation in many systems. [62–66] Although it has been provided a viable approach to improve device performance, the interfacial electron transfer dynamics of the core/shell design have not been investigated extensively. Recently in Dempsey group, two competitive recombination mechanisms have been elucidated as the first quantified investigation on back electron transfer kinetics in SnO$_2$/TiO$_2$ core/shell material. [67] Transient absorption spectroscopy was utilized to explore the effect of shell thickness on interfacial BET dynamics.

The flatband potential of metal oxide semiconductors is determined by the proton concentration at the semiconductor-electrolye interface in aqueous environment. The

effect of protonation/deprotonation equilibrium at the semiconductor surface attributes flatband potential shifting, following Nernstian dependency of -59 mV/pH unit. [68,69] The pH-dependent flatband potential movement changes the degree of overlap between the donor sensitizer excited state distribution function and semiconductor acceptor state, resulting in sensitized photocurrent efficiency. [70] Regarding pH dependency in recombination dynamics, it has been explored in ruthenium dye sensitized nanocrystalline SnO_2 and TiO_2 using transient absorption spectroscopy and complementary electrochemical measurements to provide the insight into the energetic distribution of sub-band-gap trap states. Both papers suggested that the observed faster back electron transfer rates for $RuP-SnO_2$ and $RuP-TiO_2$ at lower pH are due to increased occupation of shallow trap sites.[71,72]

The goal of this study is to investigate pH dependency on interfacial back electron transfer dynamics in SnO_2/TiO_2 core/shell structure. Transient absorption spectroscopy along with electrochemical tools will allow us to provide valuable insights on core/shell energy band structure in different pH environment.
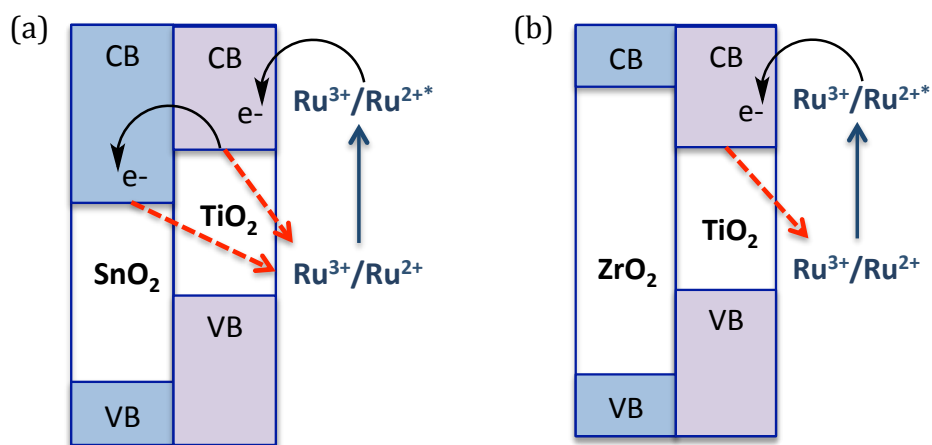
Scheme 2.1. Schematics of conduction band energies of the core/shell structure.

2.1. Experimental Methods

2.1.1. Nanocrystalline SnO$_2$ and ZrO$_2$ film fabrication

To prepare SnO2 colloidal paste, 1 mL acetic acid was added to 30 mL of 15 wt

% SnO2 colloidal dispersion in water (Alfa Aesar) and the mixture was stirred overnight

at room temperature. This solution underwent hydrothermal treatment using a Parr

Instruments pressure vessel at 240 °C for 60 h. The resulting solution was then sonicated

and 2.5 wt % of both polyethylene oxide (mol wt 100,000) and polyethylene glycol (mol

wt 12,000) was added. Stirring for 12 h yielded a homogeneous colloidal paste.

Transparent thin-film electrodes were prepared by depositing the sol–gel paste onto

conductive FTO glass substrates 4 cm × 2.2 cm using the doctor blade method with tape

casting and sintered at 450 °C for 30 min under air.[71] Nanocryatalline ZrO2 films were

prepared using a previously reported procedure. [73]

2.1.2. Atomic layer deposition of TiO$_2$ shells

      TDMAT precursor in UNC

Atomic layer deposition (ALD) was performed in a commercial reactor (Savannah

S200, Cambridge Nanotech). Titanium dioxide (TiO2) was deposited using Tetrakis

(dimethylamido) titanium, Ti(NMe2)4 (TDMAT, 99.999%, Sigma-Aldrich), and water.

The reactor temperature was 130 °C. The TDMAT reservoir was kept at 75 °C. The

TDMAT was pulsed into the reactor for 0.3 s and then held for 10 s before opening the

pump valve and purging for 10 s. Deposit conditions were 130 °C and 20 torr of N2

carrier gas with a sequence of 0.3-s metal precursor dose, 10-s hold, 20-s N2 purge, 0.02-

s H_2O dose, 10-s hold, 20-s N_2 purge.

TiCl$_4$ precursor in NCSU[67]

Atomic layer deposition was conducted in a custom-built, hot walled, flow tube reactor described previously. Reactant precursor gases, including TiCl$_4$ (99%, Strem Chemicals) and reagent grade water (Ricca Chemicals), were delivered to the reactor though heated gas lines using nitrogen carrier flow (99.999% purity, National Welders) further purified (Entegris Gate-Keeper) to reduce water contamination. The reactor was configured with gate valves to isolate the deposition zone, allowing the deposition substrate to receive extended exposure or "hold" steps to promote precursor diffusion throughout the inorganic oxide nanoparticle films. Deposition was performed at 120 °C. Precursor gas flow timing was controlled electronically by a LabVIEW sequencer to achieve dose/hold/purge steps of 0.3/ 60/180 s, respectively, for the TiCl$_4$ and water reactants.

2.1.3. Surface loading of SnO$_2$/TiO$_2$-RuP and ZrO$_2$/TiO$_2$-RuP films

All films were fully loaded by soaking 6 hours in 0.1 M HClO$_4$ aqueous solutions containing RuP (1×10^{-5}–2×10^{-4} M). Slides were then soaked for 1 h in aqueous 0.1 M HClO$_4$ solution to remove excess unanchored chromophores. Absorbance measurements of the films were performed using a Cary 60 absorbance spectrophotometer.

2.1.4. Transient absorption spectroscopy

All samples utilized in transient absorption measurements were prepared in 0.1 M LiClO$_4$ aqueous HClO$_4$ solution in 10 mm pathlength, air-tight quartz cuvettes. The

loaded slides were placed in a cuvette at a 45 angle to the beam direction and samples were purged with N_2 for at least 40 min prior to experimentation. Transient absorption experiments were performed using a custom-built laser flash photolysis system. Laser excitation (5-7 ns FWHM, 10 Hz, Q-switched) was provided by the third harmonic of a Nd:YAG laser (Spectra-Physics, Inc., model Quanta-Ray LAB-170-10) that pumped an OPO (basiScan, GWU Lasertechnik) to access tunable excitation (415–800 nm). Laser power at the sample cuvette was attenuated by the use of a half waveplate (WPMH10M-355, ThorLabs) and polarizer (GL10-A, ThorLabs). A glass window was used to deflect a small portion of excitation beam to a Si diode detector (DET10A, ThorLabs), triggering the oscilloscope to start data collection. Timing of the laser was controlled by a digital delay generator (9514+ Pulse Generator, Quantum Composers).

A 75 watt Xe Arc Lamp (PowerArc, Optical Building Blocks) was used in continuous wave mode as a white light source. The probe beam was passed through a 375 nm long pass filter before passing through the sample collinear with the pump beam. Probe light was then attenuated using a neutral density filter, and scatted excitation light is filtered with a color filter wheel containing various long pass and short pass filters. Single wavelength kinetics were obtained using a double slit monochomator (Spectral Products CM112) outfitted with a Hamamatsu R928 photomultiplier tube (PMT). The signal was amplified by a 200 MHz wideband voltage amplifier (DHPVA-200, Electro Optical Components), and processed using a digitizer (CompuScope 12502, GaGeScope) controlled by custom software (MATLAB). The data were converted to units of ΔOD ($\Delta OD = -\log(I/I_0)$, where I is the time-resolved probe light intensity with laser excitation,

and I_0 is the intensity without excitation). Data was further analyzed in Igor Pro 6.22 (Wavemetrics).

2.2. Results

2.2.1. Atomic layer deposition and characterization of RuP-SnO$_2$/TiO$_2$ films

We have prepared core/shell materials from two different facilities in UNC and NCSU, where utilizing two different TiO$_2$ precursors. One is TDMAT, tetrakis(dimethylamido) titanium, in UNC CHANL lab, and the other is TiCl$_4$ in NCSU. All of data conducted in this study (except for Figure 1 data) were the samples fabricated using TiCl$_4$ reactant precursor.

Conformal shells of TiO$_2$ were deposited on nanocrystalline SnO$_2$ and ZrO$_2$ slides using atomic layer deposition. TiO$_2$ shell thicknesses were controlled by altering the number of ALD cycles and further confirmed using ellipsometry on the witness silicon substrates. The growth rate per cycle was measured by spectroscopic ellipsometry on silicon wafers and the liner plot of thickness vs. cycle number gave 0.71 Å /cycle. (Figure 1-a) Then the prepared SnO$_2$/TiO$_2$ and ZrO$_2$/TiO$_2$ films were loaded with phosphonate-functionalized ruthenium chromophore [Ru(bpy)$_2$(4,4'-(PO$_3$H$_2$)bpy)]$^{2+}$ (RuP). As seen in Figure 1-b, MLCT band of RuP dye appears distinctively, although the background absorbance increase with TiO$_2$ thickness from scattering and background TiO$_2$ absorbance. However, the extent of loaded dye decreases with increasing the shell thickness in thicker shell passing over 5 nm, consistent with a reduction in surface area upon atomic layer deposition.

(a)

(b)
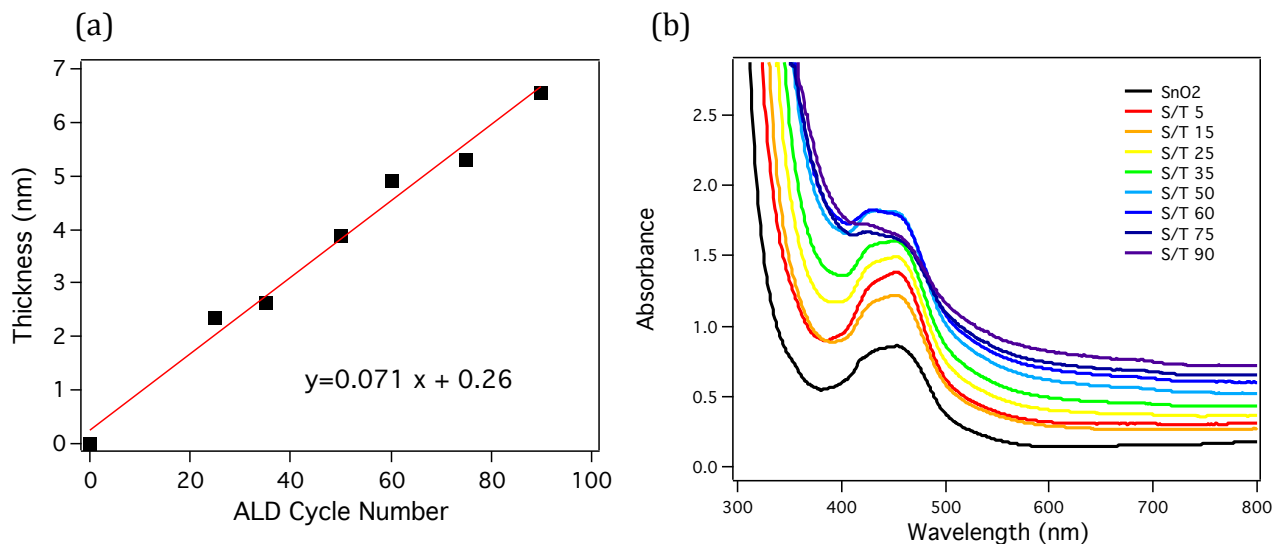
Figure 2.1. (a) Thickness of the TiO$_2$ deposited on SiO$_2$ substrates against the number of ALD cycles. Linearity was verified, yielding 0.71 Å per cycle growth rate. (b) Absorption spectra of RuP-sensitized SnO$_2$/TiO$_2$ core/shell films.

2.2.2. Interfacial charge recombination dynamics

Absorption-time traces monitored at 400 nm following 480 nm excitation of SnO$_2$/TiO$_2$-RuP in HClO$_4$ at pH 1, 3, and 5 are shown in Figure 2. Importantly, excitation pulse energies were varied in order to achieve equivalent injection yields between samples by conducting the same magnitude of bleach.
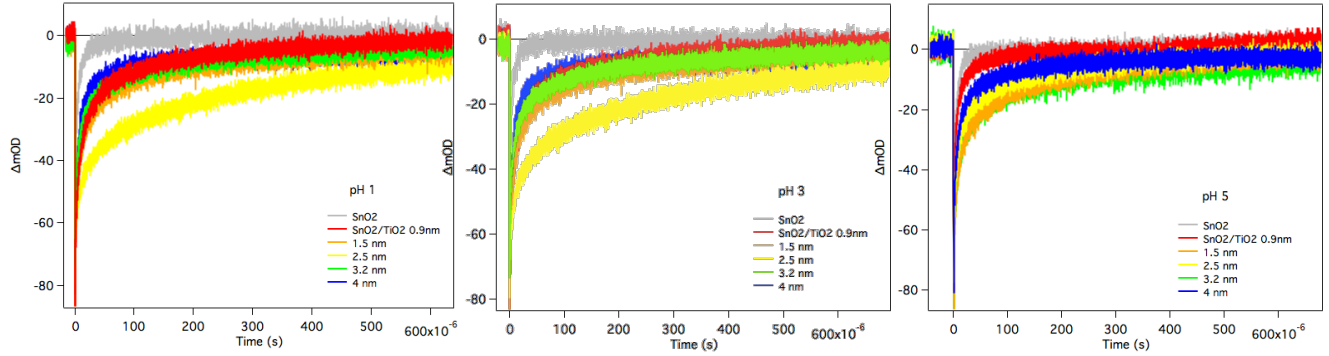
Figure 2.2. Transient absorption kinetics of RuP sensitized SnO_2/TiO_2 at 400 nm in pH 1 (left), pH 3 (middle), and pH 5 (right) $HClO_4$ solutions at various amorphous TiO_2 thicknesses. Pulse energies are varied to obtain the same bleach at the first observation point. ($\lambda_{ex} = 480$ nm)

Figure 3 is the compiled data in Figure 2, showing the dependence of $\tau_{1/2}$ on TiO_2 shell thickness for SnO_2/TiO_2 core/shell films at equal injection yields at pH 1, pH 3, and pH 5 solutions. As the shell thickness is increased from 0 to 2.5 nm, recombination time increases by 1 to 2 orders of magnitudes, depending on proton concentration in the solution. Increased $\tau_{1/2}$ values obtained as a function of pH were: 359 ns to 18.8 us (pH 1), 382 ns to 8.7 us (pH 3), and 580 ns to 6.2 us (pH 5). However, recombination begins to accelerate as the amorphous TiO_2 shells thickness exceeds 2.5 nm, and then $\tau_{1/2}$ levels at thicker shell samples.

In case of bare SnO_2 samples (no TiO_2 shell), the rate of recombination is attenuated as the pH is increased from pH 1 to pH 5. Such pH dependence trend has been observed in previous studies of RuP-SnO_2 and RuP-TiO_2 systems. [71,72] Interestingly, as

36

the TiO_2 shell thickness reaches to 2.5 nm, pH dependence reveals completely opposite

tendency. A clear dependence appears in Figure 4, with faster back electron transfer as

the pH is increasing. For thicker TiO_2 shells examined, the recombination dynamics

become pH independent.
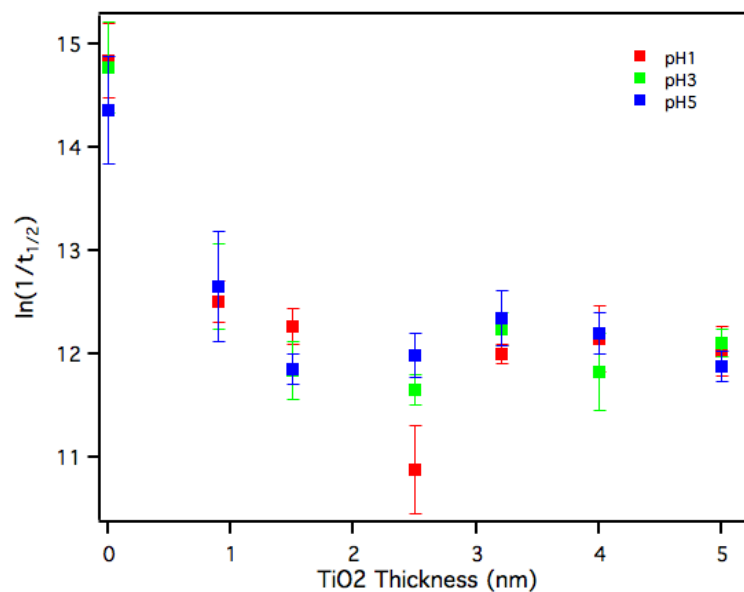
Figure 2.3. Plot of $\ln(1/\tau_{1/2})$ vs TiO_2 thickness for SnO_2/TiO_2 films at equal injection

yields in pH 1 (red), pH 3 (green) and pH 5 (blue) solutions. Collected data were

averaged from three sets of measurement.
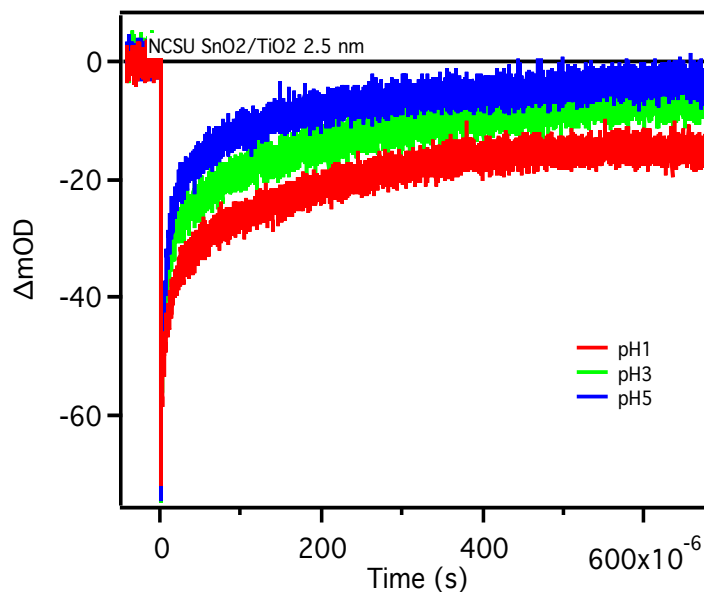
Figure 2.4. Transient absorption kinetics traces of RuP-SnO$_2$/TiO$_2$ (2.5 nm TiO$_2$ shell) films at 400 nm in pH 1 (red), pH 3 (green) and pH 5 (blue) solutions. (λ_{ex} = 480 nm)

Kinetics of recombination were also measured for ZrO$_2$/TiO$_2$-RuP films, which served as control samples. The conduction band potential of ZrO$_2$ is 0.9 V more negative than the conduction band of TiO$_2$.[59] These control experiments allow us to isolate the BET localized in the TiO$_2$ shell as the electrons inject into the TiO$_2$ shell but cannot localize in the ZrO$_2$ core. (Scheme 1) Figures 5 show TiO$_2$ shell thickness dependence of recombination kinetics in pH 1, 3, and 5 at equal injection yield in ZrO$_2$/TiO$_2$-RuP samples. As the TiO$_2$ shell increases from 0.9 to 4 nm, $\tau_{1/2}$ increases 1 fold of magnitude. As shell thickness is increased further 3.2 and 4 nm, $\tau_{1/2}$ plateaus. A higher density of shell acceptor states is expected to attenuate the rate of BET if recombination of injected electrons occur via a site-to-site hopping or trapping/detrapping mechanism.[71,74] The

similarity of BET converge between SnO_2/TiO_2 and ZrO_2/TiO_2 films suggests the recombination proceeds by a parallel mechanism in thicker shell samples.

2.3. Discussions

Based on the staggered band energetics of SnO_2 and TiO_2, an injected electron will localize in the core SnO_2 conduction band and recombine with oxidized dye through tunneling mechanism (Scheme 1). The rate of electron tunneling through a barrier depends on barrier thickness (d) and the barrier height (ΔE). The rate constant k_{ET} will attenuate exponentially with increasing tunneling distance and thickness following equation (1).

$$k_{ET} = k^\circ_{ET} \, e^{-\beta d} \qquad (1)$$

The tunneling decay constant β describes the steepness of the exponential decrease and reflects the square barrier height.[75,76] Compared to the donor-bridge-acceptor molecular systems in a well-defined matrix, tunneling mechanism in core/shell materials has been less extensively studied. For core/shell systems, BET dynamics must be considered both recombination processes of electron localized in the core and that of trapped electron in the shell.

Before analyzing pH dependent behavior of recombination kinetics in SnO_2/TiO_2 samples, the plots of Figure 3 must be deconvoluted with ZrO_2/TiO_2 control samples to differentiate the BET from electrons localized in the trap state in the TiO_2 shell.
In order to determine the contribution of tunneling and shell recombination processes as the function of shell thickness, we adopted the modeling method presented in the previous paper by Knauf.[67] Equation 2 describes the linear relationship between $\ln(1/\tau_{1/2})$

and TiO$_2$ shell thickness for recombination via electron tunneling kinetics, where k°$_{ET}$ is BET rate in no TiO$_2$ structure. The recombination from the electrons localized in TiO$_2$ shell is expressed with equation 3, which was plotted with empirical sigmoidal fit of ln(1/$\tau_{1/2}$) vs TiO$_2$ thickness from the ZrO$_2$/TiO$_2$ data in pH 1, 3, and 5 solutions (Figures 5). These two mechanisms are then plotted with weighting functions that varied from 0 to 1 to obtain the analytical insight into the contribution of each mechanism to the overall observed recombination kinetics at each shell thickness sample, expressed in equation 4.

$$f_{\text{tunnel}}(x) = -\beta x + \ln(k°_{ET}) \tag{2}$$

$$f_{\text{shell, pH1}}(x) = 14.768 + \frac{-2.343}{1+exp(2.703\,(1.619-x))} \tag{3}$$

$$f_{\text{shell, pH3}}(x) = 14.192 + \frac{-2.321}{1+exp(3.282\,(2.626-x))}$$

$$f_{\text{shell, pH5}}(x) = 14.096 + \frac{-2.046}{1+exp(4.260\,(2.614-x))}$$

$$f_{\text{obs}}(x) = f_{\text{tunnel}}(x)\left(\frac{1}{1+exp\,(k(x-Xh))}\right) + f_{\text{shell}}(x)\left(\frac{1}{1+exp\,(-k(x-Xh))}\right) \tag{4}$$
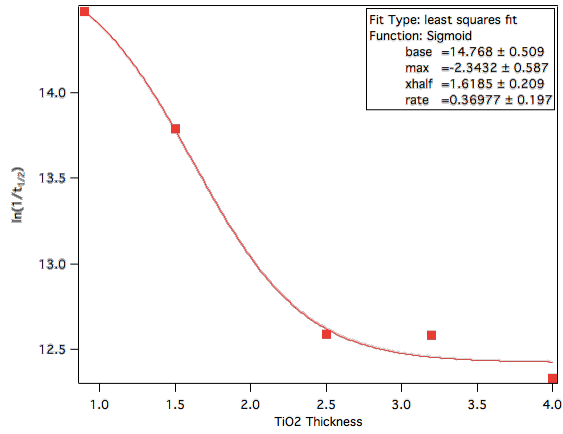
$$f_{\text{shell, pH1}}(x) = 14.768 + \frac{-2.343}{1 + exp(2.703\,(1.619-x))}$$
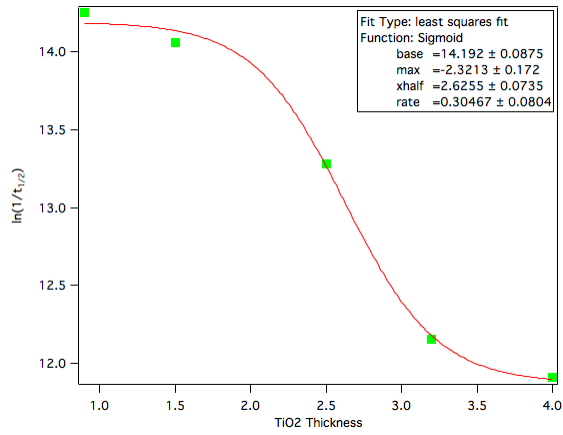
$$f_{\text{shell, pH3}}(x) = 14.192 + \frac{-2.321}{1 + exp(3.282\,(2.626-x))}$$
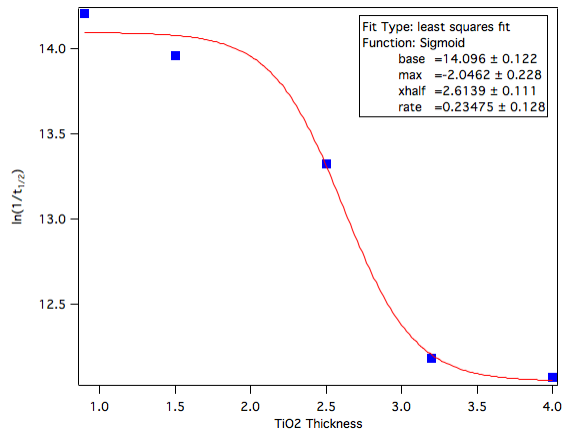
$$f_{\text{shell, pH5}}(x) = 14.096 + \frac{-2.046}{1 + exp(4.260\,(2.614-x))}$$

Figure 2.5. Plot of $\ln(1/\tau_{1/2})$ vs TiO_2 thickness for ZrO_2/TiO_2 films at equal injection yields in pH 1 (top), pH 3 (middle) and pH 5 (bottom) solutions. The fit empirically models the back electron transfer from localized shell with sigmoid functions.

41

β values (tunneling component) and X_h (intersection of two sigmoid) have been determined after fitting the SnO_2/TiO_2 data of Figure 5, using the equation 4 in each pH solution. Spectra in Figure 6 contain the obtained fitting spectra as black lines and the values of β and X_h in the inset box; β = 0.20 $Å^{-1}$ and X_h = 2.61 nm in pH 1, β = 0.22 $Å^{-1}$ and X_h = 2.33 nm in pH 3, and β = 0.19 $Å^{-1}$ and X_h = 2.28 nm in pH 5. Even though there were not enough data points to yield reliable results, those seem reasonable values, compared to β = 0.25 $Å^{-1}$ and X_h = 3.2 nm in previous study. [67]

A decreasing sigmoid at the weighting function shows tunneling component from SnO_2 core because at small TiO_2 thicknesses, tunneling is the dominant process for BET; thus, its contribution would decrease with increased TiO_2 thickness. The complementary sigmoid is used as a shell recombination mechanism in weighting function, which exhibited as the primary process at thick shells. The intersection of these two sigmoidal functions is defined with parameter X_h, where the dominant mechanism switches from tunneling to the shell localized recombination. The sigmoidal weight functions from the analysis of the equal injection yield data in pH 1, 3, and 5 were collected in Figure 7. Since the β value is proportional to the energy barrier for electron tunneling, different β will likely reveal different conduction band edge energies of TiO_2 shell. Regarding β parameters obtained in different pH aqueous $HClO_4$ solutions, β = 0.20 $Å^{-1}$ in pH 1, 0.22 $Å^{-1}$ in pH 3, and 0.19 $Å^{-1}$ in pH 5, it is hard to say their values are in the range of experimental error or they are exhibiting the independent behavior on various pH environment. In comparison, there is a discernible trend in X_h values, where the major recombination process switches from core tunneling to the shell BET. Based on the X_h yielded from the empirical fitting, 2.61 nm in pH 1, 2.33 nm in pH 3, and 2.28 nm in pH

5, it has a smaller X_h at higher pH. It is hard to interpret this result relevantly to the density of states in different pH by using the transient absorption spectroscopy as the only tool. Further investigation such as electrochemical measurements of SnO_2/TiO_2 core/shell material in different pH should be accompanied to understand this preliminary examination.
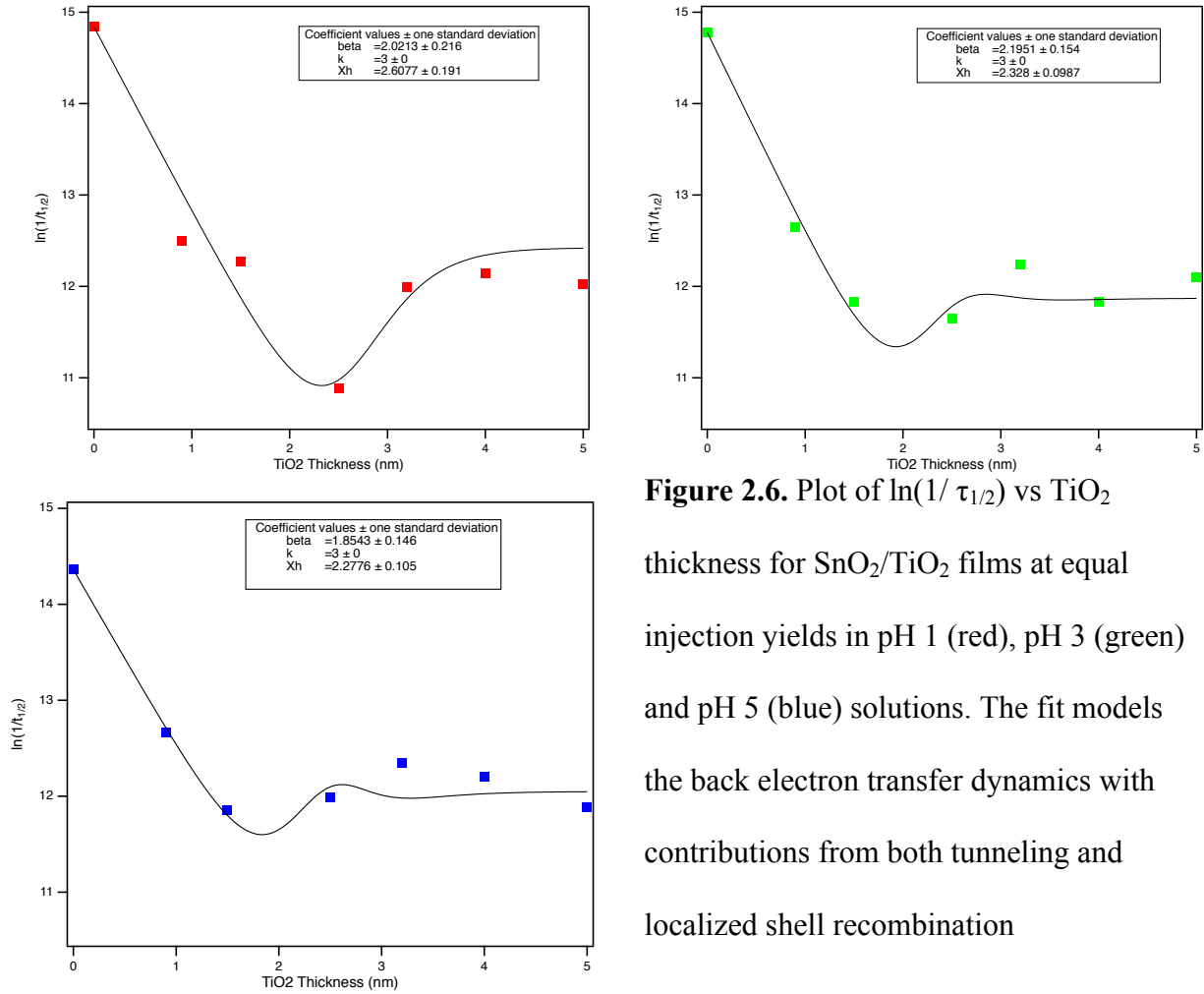
Figure 2.6. Plot of $\ln(1/\tau_{1/2})$ vs TiO_2 thickness for SnO_2/TiO_2 films at equal injection yields in pH 1 (red), pH 3 (green) and pH 5 (blue) solutions. The fit models the back electron transfer dynamics with contributions from both tunneling and localized shell recombination
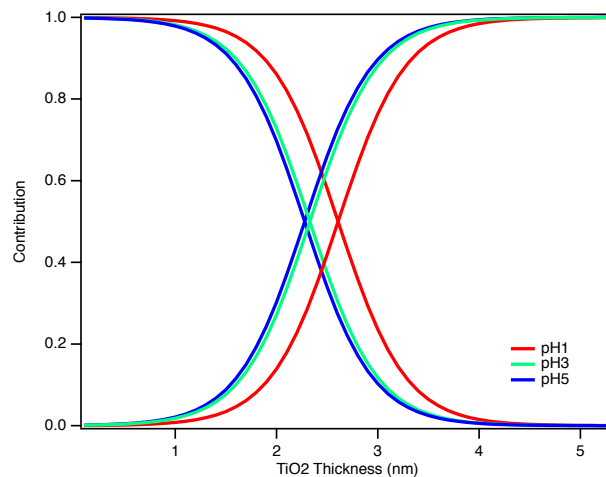
Figure 2.7. Sigmoidal weighting functions from the fitting of equal injection data of pH 1 (red), pH 3 (green) and pH 5 (blue) samples.

Table 2.1. β values (tunneling component) and X_h (intersection of two sigmoid) determined in pH 1, 3, and 5.

	pH 1	**pH 3**	**pH 5**
β	0.20 Å^{-1}	0.22 Å^{-1}	0.19 Å^{-1}
X_h	2.61 nm	2.33 nm	2.28 nm

2.4. Conclusions and Future Directions

Interfacial charge recombination dynamics in amorphous SnO_2/TiO_2 core/shell system were investigated using transient absorption spectroscopy in pH 1, 3, and 5. We revisited the effect of shell thickness on BET processes; two competitive mechanisms of core tunneling electron transfer and shell-localized recombination become predominant depending on the shell thickness. After isolating shell recombination process, we were able to obtain tunneling parameters and X_h as a function of pH. Together with spectroscopic data, electrochemical analysis must be accompanied in near future to fully understand pH effects on interfacial dynamics in core/shell structure. Additionally, it would be worth to explore the interfacial dynamics at TDMAT precursor-deposited core/shell samples and annealed samples as well.

REFERENCES

(1) Ooyama, Y.; Nagano, T.; Inoue, S.; Imae, I.; Komaguchi, K.; Ohshita, J.; Harima, Y. *Chem. - A Eur. J.* **2011**, *17* (52), 14837.

(2) Odobel, F.; Pellegrin, Y.; Gibson, E. a.; Hagfeldt, A.; Smeigh, A. L.; Hammarström, L. *Coord. Chem. Rev.* **2012**, *256* (21–22), 2414.

(3) Dini, D.; Halpin, Y.; Vos, J. G.; Gibson, E. A. *Coord. Chem. Rev.* **2015**, *304–305*, 179.

(4) Wood, C. J.; Summers, G. H.; Clark, C. A.; Kaeffer, N.; Braeutigam, M.; Carbone, L. R.; D'Amario, L.; Fan, K.; Farré, Y.; Narbey, S.; Oswald, F.; Stevens, L. A.; Parmenter, C. D. J.; Fay, M. W.; La Torre, A.; Snape, C. E.; Dietzek, B.; Dini, D.; Hammarström, L.; Pellegrin, Y.; Odobel, F.; Sun, L.; Artero, V.; Gibson, E. A. *Phys. Chem. Chem. Phys.* **2016**, *18* (16), 10727.

(5) Flynn, C. J.; Oh, E. E.; McCullough, S. M.; Call, R. W.; Donley, C. L.; Lopez, R.; Cahoon, J. F. *J. Phys. Chem. C* **2014**, *118* (26), 14177.

(6) Flynn, C. J.; McCullough, S. M.; Oh, E.; Li, L.; Mercado, C. C.; Farnum, B. H.; Li, W.; Donley, C. L.; You, W.; Nozik, A. J.; McBride, J. R.; Meyer, T. J.; Kanai, Y.; Cahoon, J. F. *ACS Appl. Mater. Interfaces* **2016**, *8* (7), 4754.

(7) Natu, G.; Hasin, P.; Huang, Z.; Ji, Z.; He, M.; Wu, Y. *ACS Appl. Mater. Interfaces* **2012**, *4* (11), 5922.

(8) Natu, G.; Huang, Z.; Ji, Z.; Wu, Y. *Langmuir* **2012**, *28* (1), 950.

(9) Uehara, S.; Sumikura, S.; Suzuki, E.; Mori, S. *Energy Environ. Sci.* **2010**, *3* (5), 641.

(10) Flynn, C. J.; McCullough, S. M.; Li, L.; Donley, C. L.; Kanai, Y.; Cahoon, J. F. *J. Phys. Chem. C* **2016**, *120* (30), 16568.

(11) Ji, Z.; Natu, G.; Huang, Z.; Kokhan, O.; Zhang, X.; Wu, Y. *J. Phys. Chem. C* **2012**, *116* (32), 16854.

(12) Ji, Z.; Wu, Y. *J. Phys. Chem. C* **2013**, *117* (36), 18315.

(13) He, M.; Ji, Z.; Huang, Z.; Wu, Y. *J. Phys. Chem. C* **2014**, *118* (30), 16518.

(14) Freys, J. C.; Gardner, J. M.; D'Amario, L.; Brown, A. M.; Hammarström, L. *Dalt. Trans.* **2012**, *41* (42), 13105.

(15) Gennari, M.; Légalité, F.; Zhang, L.; Pellegrin, Y.; Blart, E.; Fortage, J.; Brown,

A. M.; Deronzier, A.; Collomb, M.-N.; Boujtita, M.; Jacquemin, D.; Hammarström, L.; Odobel, F. *J. Phys. Chem. Lett.* **2014**, *5* (13), 2254.

(16)   Warnan, J.; Gardner, J.; Le Pleux, L.; Petersson, J.; Pellegrin, Y.; Blart, E.; Hammarström, L.; Odobel, F. *J. Phys. Chem. C* **2014**, *118* (1), 103.

(17)   Nattestad, a; Mozer, a J.; Fischer, M. K. R.; Cheng, Y.-B.; Mishra, A.; Bäuerle, P.; Bach, U. *Nat. Mater.* **2010**, *9* (1), 31.

(18)   Morandeira, A.; Fortage, J.; Edvinsson, T.; Le Pleux, L.; Blart, E.; Boschloo, G.; Hagfeldt, A.; Hammarström, L.; Odobel, F. *J. Phys. Chem. C* **2008**, *112* (5), 1721.

(19)   Le Pleux, L.; Smeigh, A. L.; Gibson, E.; Pellegrin, Y.; Blart, E.; Boschloo, G.; Hagfeldt, A.; Hammarström, L.; Odobel, F. *Energy Environ. Sci.* **2011**, *4* (6), 2075.

(20)   Wood, C. J.; Cheng, M.; Clark, C. A.; Horvath, R.; Clark, I. P.; Hamilton, M. L.; Towrie, M.; George, M. W.; Sun, L.; Yang, X.; Gibson, E. a. *J. Phys. Chem. C* **2014**, *118* (30), 16536.

(21)   Gibson, E. A.; Smeigh, A. L.; Le Pleux, L.; Fortage, J.; Boschloo, G.; Blart, E.; Pellegrin, Y.; Odobel, F.; Hagfeldt, A.; Hammarström, L. *Angew. Chemie Int. Ed.* **2009**, *48* (24), 4402.

(22)   Qin, P.; Zhu, H.; Edvinsson, T.; Boschloo, G.; Hagfeldt, A.; Sun, L. *J. Am. Chem. Soc.* **2008**, *130* (27), 8570.

(23)   Qin, P.; Wiberg, J.; Gibson, E. a.; Linder, M.; Li, L.; Brinck, T.; Hagfeldt, A.; Albinsson, B.; Sun, L. *J. Phys. Chem. C* **2010**, *114* (10), 4738.

(24)   Gibson, E. A.; Smeigh, A. L.; Le Pleux, L.; Hammarström, L.; Odobel, F.; Boschloo, G.; Hagfeldt, A. *J. Phys. Chem. C* **2011**, *115* (19), 9772.

(25)   Liu, Z.; Li, W.; Topa, S.; Xu, X.; Zeng, X.; Zhao, Z.; Wang, M.; Chen, W.; Wang, F.; Cheng, Y.-B.; He, H. *ACS Appl. Mater. Interfaces* **2014**, *6* (13), 10614.

(26)   Powar, S.; Daeneke, T.; Ma, M. T.; Fu, D.; Duffy, N. W.; Götz, G.; Weidelener, M.; Mishra, A.; Bäuerle, P.; Spiccia, L.; Bach, U. *Angew. Chemie Int. Ed.* **2013**, *52* (2), 602.

(27)   Perera, I. R.; Daeneke, T.; Makuta, S.; Yu, Z.; Tachibana, Y.; Mishra, A.; Bäuerle, P.; Ohlin, C. A.; Bach, U.; Spiccia, L. *Angew. Chemie Int. Ed.* **2015**, *54* (12), 3758.

(28)   Cui, J.; Lu, J.; Xu, X.; Cao, K.; Wang, Z.; Alemu, G.; Yuang, H.; Shen, Y.; Xu, J.; Cheng, Y.; Wang, M. *J. Phys. Chem. C* **2014**, *118* (30), 16433.

(29) Weidelener, M.; Mishra, A.; Nattestad, A.; Powar, S.; Mozer, A. J.; Mena-Osteritz, E.; Cheng, Y.-B.; Bach, U.; Bäuerle, P. *J. Mater. Chem.* **2012**, *22* (15), 7366.

(30) Warnan, J.; Pellegrin, Y.; Blart, E.; Zhang, L.; Brown, A.; Hammarström, L.; Jacquemin, D.; Odobel, F. *Dye. Pigment.* **2014**, *105*, 174.

(31) Bian, Z.; Tachikawa, T.; Cui, S.-C.; Fujitsuka, M.; Majima, T. *Chem. Sci.* **2012**, *3* (2), 370.

(32) Ardo, S.; Meyer, G. J. *Chem. Soc. Rev.* **2009**, *38* (1), 115.

(33) Robertson, N. *Angew. Chemie Int. Ed.* **2006**, *45* (15), 2338.

(34) Bomben, P. G.; Thériault, K. D.; Berlinguette, C. P. *Eur. J. Inorg. Chem.* **2011**, *2011* (11), 1806.

(35) Argazzi, R.; Murakami Iha, N. Y.; Zabri, H.; Odobel, F.; Bignozzi, C. A. *Coord. Chem. Rev.* **2004**, *248* (13–14), 1299.

(36) Ji, Z.; Natu, G.; Huang, Z.; Kokhan, O.; Zhang, X.; Wu, Y. *J. Phys. Chem. C* **2012**, *116* (32), 16854.

(37) Ji, Z.; Natu, G.; Wu, Y. *ACS Appl. Mater. Interfaces* **2013**, *5* (17), 8641.

(38) Lyu, S.; Farré, Y.; Ducasse, L.; Pellegrin, Y.; Toupance, T.; Olivier, C.; Odobel, F. *RSC Adv.* **2016**, *6* (24), 19928.

(39) Thompson, D. W.; Ito, A.; Meyer, T. J. *Pure Appl. Chem.* **2013**, *85* (7), 1257.

(40) Bräutigam, M.; Kübel, J.; Schulz, M.; Vos, J. G.; Dietzek, B. *Phys. Chem. Chem. Phys.* **2015**, *17* (12), 7823.

(41) Sulliva, B. P.; Salmon, D. J.; Meyer, T. J. *Inorg. Chem.* **1978**, *17* (12), 3334.

(42) Chan, K. S.; Tse, A. K.-S. *Synth. Commun.* **1993**, *23* (14), 1929.

(43) Xia, H.; Zhu, Y.; Lu, D.; Li, M.; Zhang, C.; Yang, B.; Ma, Y. *J. Phys. Chem. B* **2006**, *110* (37), 18718.

(44) Song, W.; Glasson, C. R. K.; Luo, H.; Hanson, K.; Brennaman, M. K.; Concepcion, J. J.; Meyer, T. J. *J. Phys. Chem. Lett.* **2011**, 1808.

(45) Hanson, K.; Brennaman, M. K.; Ito, A.; Luo, H.; Song, W.; Parker, K. A.; Ghosh, R.; Norris, M. R.; Glasson, C. R. K.; Concepcion, J. J.; Lopez, R.; Meyer, T. J. *J. Phys. Chem. C* **2012**, *116* (28), 14837.

(46)   Gallagher, L. a; Serron, S. a; Wen, X.; Hornstein, B. J.; Dattelbaum, D. M.; Schoonover, J. R.; Meyer, T. J. *Inorg. Chem.* **2005**, *44* (6), 2089.

(47)   Ito, S.; Murakami, T. N.; Comte, P.; Liska, P.; Grätzel, C.; Nazeeruddin, M. K.; Grätzel, M. *Thin Solid Films* **2008**, *516* (14), 4613.

(48)   McFarland, S. a.; Lee, F. S.; Cheng, K. a W. Y.; Cozens, F. L.; Schepp, N. P. *J. Am. Chem. Soc.* **2005**, *127* (19), 7065.

(49)   Pearson, P.; Bond, A. M.; Deacon, G. B.; Forsyth, C.; Spiccia, L. *Inorganica Chim. Acta* **2008**, *361* (3), 601.

(50)   Liu, F.; Meyer, G. J. *Inorg. Chem.* **2005**, *44* (25), 9305.

(51)   Furue, M.; Maruyama, K.; Oguni, T.; Naiki, M.; Kamachi, M. *Inorg. Chem.* **1992**, *31* (18), 3792.

(52)   Wolfbauer, G.; Bond, A. M.; Deacon, G. B.; MacFarlane, D. R.; Spiccia, L. *J. Am. Chem. Soc.* **2000**, *122* (1), 130.

(53)   Heuer, W. B.; Xia, H.-L.; Ward, W.; Zhou, Z.; Pearson, W. H.; Siegler, M. A.; Narducci Sarjeant, A. A.; Abrahamsson, M.; Meyer, G. J. *Inorg. Chem.* **2012**, *51* (7), 3981.

(54)   Scaltrito, D. V.; Thompson, D. W.; O'Callaghan, J. a.; Meyer, G. J. *Coord. Chem. Rev.* **2000**, *208* (1), 243.

(55)   He, J.; Lindström, H.; Hagfeldt, A.; Lindquist, S.-E. *J. Phys. Chem. B* **1999**, *103* (42), 8940.

(56)   Crutchley, R. J.; Lever, a. B. P. *J. Am. Chem. Soc.* **1980**, *102* (23), 7128.

(57)   Nelsen, S. F.; Hintz, P. J. *J. Am. Chem. Soc.* **1972**, *94* (20), 7114.

(58)   Farnum, B. H.; Jou, J. J.; Meyer, G. J. *Proc. Natl. Acad. Sci. U. S. A.* **2012**, *109*, 15628.

(59)   Sayama, K.; Arakawa, H. *J. Phys. Chem.* **1993**, *97* (3), 531.

(60)   McCusker, J. K. *Acc. Chem. Res.* **2003**, *36* (12), 876.

(61)   Morandeira, A.; Boschloo, G.; Hagfeldt, A.; Hammarström, L. *J. Phys. Chem. B* **2005**, *109* (41), 19403.

(62)   Alibabaei, L.; Sherman, B. D.; Norris, M. R.; Brennaman, M. K.; Meyer, T. J. *Proc. Natl. Acad. Sci.* **2015**, *3* (23), 201506111.

(63)   Alibabaei, L.; Farnum, B. H.; Kalanyan, B.; Brennaman, M. K.; Losego, M. D.; Parsons, G. N.; Meyer, T. J. **2014**.

(64)   Wee, K.-R.; Sherman, B. D.; Brennaman, M. K.; Sheridan, M. V.; Nayak, A.; Alibabaei, L.; Meyer, T. J. *J. Mater. Chem. A* **2016**, *4* (8), 2969.

(65)   Sherman, B. D.; Ashford, D. L.; Lapides, A. M.; Sheridan, M. V.; Wee, K.-R.; Meyer, T. J. *J. Phys. Chem. Lett.* **2015**, *6* (16), 3213.

(66)   Kay, A.; Gratzel, M. *chem. mater.* **2002**, *14*, 2930.

(67)   Knauf, R. R.; Kalanyan, B.; Parsons, G. N.; Dempsey, J. L. *J. Phys. Chem. C* **2015**, *119* (51), 28353.

(68)   Qu, P.; Meyer, G. J. *Langmuir* **2001**, *17* (21), 6720.

(69)   Zaban, A.; Ferrere, S.; Gregg, B. a. *J. Phys. Chem. B* **1998**, *102* (2), 452.

(70)   Watson, D. F.; Meyer, G. J. *Coord. Chem. Rev.* **2004**, *248* (13–14), 1391.

(71)   Knauf, R. R.; Brennaman, M. K.; Alibabaei, L.; Norris, M. R.; Dempsey, J. L. **2013**.

(72)   Brennaman, M. K.; Patrocinio, A. O. T.; Song, W.; Jurss, J. W.; Concepcion, J. J.; Hoertz, P. G.; Traub, M. C.; Iha, N. Y. M.; Meyer, T. J. *ChemSusChem* **2011**, *4*, 216.

(73)   Ito, S.; Zakeeruddin, S. M.; Humphry-Baker, R.; Liska, P.; Charvet, R.; Comte, P.; Nazeeruddin, M. K.; Péchy, P.; Takata, M.; Miura, H.; Uchida, S.; Grätzel, M. *Adv. Mater.* **2006**, *18* (9), 1202.

(74)   Haque, S. A.; Tachibana, Y.; Willis, R. L.; Moser, J. E.; Grätzel, M.; Klug, D. R.; Durrant, J. R. *J. Phys. Chem. B* **2000**, *104* (3), 538.

(75)   Prasittichai, C.; Avila, J. R.; Farha, O. K.; Hupp, J. T. *J. Am. Chem. Soc.* **2013**, *135* (44), 16328.

(76)   Avila, J. R.; Katz, M. J.; Farha, O. K.; Hupp, J. T. *J. Phys. Chem. C* **2016**, *120* (37), 20922.